

Ukko-Ville Mäkinen

DEVELOPMENT OF AN AGGLOMERATION INLET FOR NANOPARTICLE CHEMICAL COMPOSITION ANALYSIS

Master's thesis

Engineering and natural sciences

Examiners: Asst. Prof. Panu Karjalainen and Doc. Axel Eriksson

April 2025

ABSTRACT

Ukko-Ville Mäkinen: Development of an agglomeration inlet for nanoparticle chemical composition analysis

Master's thesis

Tampere University

Science and engineering degree programme

April 2025

The chemical composition of particles is a key factor in determining their toxicological and environmental effects. The aerosol mass spectrometer (AMS) is the most utilized instrument in online aerosol chemical composition measurements. With an added soot particle module (SP), the SP-AMS can detect both refractory and non-refractory species. The particle beam of the AMS is created by an aerodynamic lens. The lens limits transmission of nanoparticles due to diffusion and micron sized particles due to inertial effects.

A previous study presented the concept of using a soot particle agglomeration inlet (SPAI) for improved detection of nanoparticles with the SP-AMS. The inlet used burner soot as agglomeration particles that were used to carry nanoparticles through the aerodynamic lens. The system was tested only on a concept level and this thesis further develops the method.

This thesis focuses on further developing the concept by finding correct operation parameters for an instrument that can be modified for different experiments. The use of an atomizer instead of a burner was a key step adopted in this thesis. Atomizers allow a range of particles to be produced with the same system, granting the ability to measure a variety of materials.

Experiments where optimal agglomeration particle distributions were generated and optimal residence times were measured were carried out for the design of the inlet system. These experiments can also be repeated in the future for other materials and act as a baseline for future development. The parts required to construct the instrument are presented with optimized flow settings and residence times.

The inlet system was validated with nanoparticles of different metals. The background signal from the agglomeration particles proved to be more substantial than expected and it interfered with some of the sampled metals. Improved detection was achieved for Ag and Zn particles using the agglomeration inlet. The SP-AMS was calibrated for these metals to achieve proper quantification. The relative ionization efficiencies of these metals were compared to other studies and showed promising results. Al and Sn had notable interference from the agglomeration particles and could not be quantified with the present system.

A thorough work of the parameters affecting the instrument allows future work to focus on finding agglomeration particles that are made from purer materials. The steps presented in this thesis can be duplicated for those materials and the same system can be run with the parameters found in this thesis. A library where mass spectra and generation guides of different materials are found is the top priority in future research on this topic.

Keywords: chemical composition, nanoparticles, aerosol mass spectrometry, instrument development

The originality of this thesis has been checked using the Turnitin OriginalityCheck service.

TIIVISTELMÄ

Ukko-Ville Mäkinen: Agglomeraatiokammion suunnittelemainen nanohiukkasten kemiallisen koostumuksen analysointiin

Diplomityö

Tampereen yliopisto

Teknis-luonnontieteellinen tutkinto-ohjelma

Huhtikuu 2025

Hiukkasten kemiallinen koostumus on avainasemassa niiden toksikologisten ja ympäristöllisten haittojen kannalta. Aerosolimassaspektrometri (AMS) on yleisin reaaliaikaiseen kemiallisen koostumuksen mittaukseen käytetty mittalaite. Lisätyn nokihiukkasmoduulin (SP) avulla SP-AMS voi mitata myös kuumuudenkestäviä aineita. Aerodynaaminen linssi luo AMS:n hiukkassuihkun. Pienimmät hiukkaset häviävät linssissä diffuusion takia ja yli mikronin kokoiset hiukkaset häviävät niiden inertian takia.

Aikaisemmassa tutkimuksessa esitettiin konsepti nokihiukkasagglomeraatiokammioista (SPAI), jolla voitiin parantaa nanohiukkasten havainnointia SP-AMS:lla. Nokihiukkasia luotiin polttimolla ja niiden pinnalle agglomeroituneet nanohiukkaset pystyttiin mittaamaan SP-AMS:lla, koska sopivan kokoiset nokihiukkaset eivät hävinneet aerodynaamiseen linssiin. Laitteen tutkimus jäi konseptitasolle ja tämä diplomityö kehittää sitä.

Tämän diplomityön keskiössä on kyseisen konseptin jatkokehittäminen löytämällä sopivat opeointiparametrit siten, että laitetta voitaisiin hyödyntää monissa sovelluksissa. Oleellisessa osassa kehityksen kannalta oli päätös vaihtaa poltin pirskonttimeen. Pirskonttimilla voidaan tuottaa monenlaisia hiukkasia, joiden avulla hyödynnyskohteita on useita.

Työn aikana mitattiin agglomeraatiohiukkasille optimaaliseen kokojakaumaan vaadittavat parametrit sekä viipymäaikakammion virtausominaisuudet, joiden avulla laite voitiin kehittää. Nämä mittaukset voidaan toistaa myös tulevaisuudessa eri materiaaleille ja ne toimivat vahvana pohjana tulevaisuuden kehitykselle. Työssä esitetään laitteen rakentamiseen vaadittavat osat ja niiden optimoidut asetukset.

Laitteen toiminta varmistettiin mittaamalla eri metallien nanohiukkasia. Taustasignaali agglomeraatiohiukkasista oli oletettua voimakkaampaa ja se häiritsi joidenkin metallien mittaamista. Hiukkasten havainnointi parani hopealle ja sinkille laitteen avulla. Näille metalleille suoritetuista kalibrointimittauksista saatuja arvoja verrattiin kirjallisuuteen ja tulokset olivat vakuuttavia. Alumiinin ja tinan mittauksessa oli huomattavia ongelmia, sillä agglomeraatiohiukkasten taustasignaalista johtuen näitä metalleja ei voitu havaita.

Laitteen toimintaan vaikuttavia parametrejä tutkittiin perusteellisesti. Tämän työn ansiosta tulevaisuudessa voidaan keskittyä sopivien agglomeraatiohiukkasten löytämiseen. Tässä diplomityössä esitetyt mittaasetelmat voidaan toistaa eri materiaaleille ja diplomityössä esitellyn laitteen osia voidaan soveltaa näiden materiaalien kanssa. Laitteen jatkotutkimuksessa tärkeintä olisi luoda kirjasto, johon eri materiaaleille löytyy ohjeet agglomeraatiohiukkasten luomiseen.

Avainsanat: kemiallinen koostumus, nanohiukkaset, aerosolimassaspektrometria, laitekehitys

Tämän julkaisun alkuperäisyys on tarkastettu Turnitin OriginalityCheck -ohjelmalla.

PREFACE

Now that this thesis is done, I would like to thank the people who helped me with this journey.

Firstly I would like to thank the Research Council of Finland project MEAPS, grant No 354226 for the funding to support this thesis. I would like to thank my supervisors Asst. Prof. Panu Karjalainen and Doc. Axel Eriksson for their help. I enjoyed our discussions about different topics regarding the thesis and learned a lot. I would also like to thank the people of Tampere university aerosol physics laboratory for their support. The good conversations during coffee breaks have been important in maintaining my motivation. I have spent a lot of time in the lab and learned much about the instrumentation that we are using and everyone has been supportive and helpful in the process.

None of this would have been possible without the support from my family and friends. I would like to thank my family for their interest in my education and for their moral support. I would like to thank my friends for great Tichu games that helped me relax and get my mind off the thesis. Most importantly I would like to thank Anni, who has supported me throughout this thesis process. Getting the thesis done without your help would not have been possible.

Tampere, 16th April 2025

Ukko-Ville Mäkinen

CONTENTS

1. Introduction	1
2. Background	3
2.1 Aerosol sources and size classification	3
2.1.1 Size distributions	3
2.1.2 Size ranges	4
2.1.3 Aerosol sources	5
2.2 Particle growth	7
2.2.1 Coagulation	7
2.2.2 Condensation	11
3. Instrument calibration	14
3.1 Particle generation	14
3.1.1 Atomizers	14
3.1.2 Tube furnaces	16
3.2 Scanning mobility particle sizer (SMPS)	17
4. Chemical composition analysis	21
4.1 Soot particle aerosol mass spectrometer (SP-AMS)	21
4.1.1 Aerodynamic lens	21
4.1.2 Time-of-flight region	26
4.1.3 Vaporization and ionization	26
4.1.4 Mass spectrum region	28
4.1.5 Calibration and data-analysis	28
4.1.6 Soot particle agglomeration inlet (SPAI)	32
4.2 Alternative methods for nanoparticle chemical composition analysis	33
5. Development and characterization	36
5.1 Development	36
5.1.1 Particle generation	37
5.1.2 Residence time	40
5.2 Design	42
5.3 Characterization	43
5.4 Future developments	48
6. Conclusions	50
References	52

LIST OF ABBREVIATIONS

AMS	Aerosol mass spectrometer
BC	Black carbon
BP	Bypass
CB	Cab-O-Jet 300
CDCE	Composition dependent collection efficiency
CIMS	Chemical ionization mass spectrometry
CMD	Count median diameter
CNC	Condensation nucleus counter
CPC	Condensation particle counter
CS	Catalytic stripper
DL	Detection limit
DMA	Differential mobility analyzer
DMPS	Differential mobility particle sizer
DV	Dual vaporizer
EC	Elemental carbon
ED	Ejector diluter
EESI	Extractive electrospray ionization
ePToF	Efficient particle time-of-flight
FIGAERO	Filter inlet for gases and aerosols
GSD	Geometric standard deviation
HR	High resolution
HR-ToF-AMS	High resolution time-of-flight aerosol mass spectrometer
ICP-MS	Inductively coupled plasma mass spectrometry
IE	Ionization efficiency
LV	Laser vaporizer
MCP	Multichannel plate
MFC	Mass flow controller

MMD	Mass median diameter
MS	Mass spectrum
NAMS	Nanoaerosol mass spectrometer
OC	Organic carbon
OFR	Oxidation flow reactor
PAH	Polycyclic aromatic hydrocarbon
PM1	Particulate matter with an aerodynamic diameter below 1 μm
PM10	Particulate matter with an aerodynamic diameter below 10 μm
PM2.5	Particulate matter with an aerodynamic diameter below 2.5 μm
PMF	Positive matrix factorization
PToF	Particle time-of-flight
RH	Relative humidity
RIE	Relative ionization efficiency
RTT	Residence time tube
SEMS	Scanning electrical mobility spectrometer
SM	Static mixer
SMD	Surface median diameter
SMPS	Scanning mobility particle sizer
SOA	Secondary organic aerosol
SP	Soot particle
SP-AMS	Soot particle aerosol mass spectrometer
SPAI	Soot particle agglomeration inlet
TD-GC/MS	Thermal desorption-gas chromatography/mass spectrometry
TEM	Transmission electron microscopy
ToF	Time-of-flight
TV	Tungsten vaporizer
UFP	Ultrafine particle
UMR	Unit mass resolution
VOC	Volatile organic compound
XEDS	X-ray energy dispersive spectrometer
XRF	X-ray fluorescence

1. INTRODUCTION

Many sources, such as traffic, industries or sea spray, emit particles to the atmosphere. These particles and their carrier gas are an example of an aerosol (Hinds 1999). Many processes evolve the particles changing their sizes or chemical compositions during their lifetime in the atmosphere. Particles may also be formed from vapors in the atmosphere via gas-to-particle conversion. (Seinfeld and Pandis 2016)

Aerosol with an aerodynamic diameter of $2.5\text{ }\mu\text{m}$ or less ($\text{PM}_{2.5}$) have been linked to adverse health effects and estimates of annual premature deaths attributed to air pollution are in the millions (Lelieveld et al. 2015; Cohen et al. 2017; Chowdhury et al. 2022). Harmful effects caused by aerosol can have an impact through multiple pathways including respiratory and cardiovascular diseases (Schraufnagel et al. 2019b). Aerosol also affect Earth's radiative budget by reflecting sunlight as particles or as cloud droplets (Forster et al. 2021).

The chemical composition of particles can greatly impact their health effects and climate impacts. Toxic species such as lead, arsenic, other metals or polycyclic aromatic hydrocarbons (PAHs) can cause illnesses (Schraufnagel et al. 2019a). Particle composition can also affect its radiative properties. Black carbon has been shown to absorb solar radiation which affects Earth's radiative budget (Booth and Bellouin 2015).

Apart from particle composition, particle size is also an important metric considering their health effects. Large particles often deposit in the upper airways while small particles are deposited in the lungs (Schraufnagel et al. 2019a). Particles with an aerodynamic diameter of less than 100 nm are called ultrafine particles (UFPs) and they can diffuse through the lipid bilayer in the lungs (Schraufnagel 2020). The combination of toxic material and a very small particle can cause extensive harm and the detailed composition of nanoparticles is needed to determine their health effects.

The aerosol mass spectrometer (AMS) is a device capable of measuring size resolved chemical composition of atmospheric particles (Jayne et al. 2000; DeCarlo et al. 2006). The AMS can detect non-refractory species (Jayne et al. 2000) and refractory species if a soot particle module (Onasch et al. 2012) is used. The AMS can distinguish individual chemical compounds due to its high mass resolution, and it can be run on a relatively short cycle to obtain data with a good time resolution (DeCarlo et al. 2006). The limiting

factor with the AMS is its inlet which is capable of transmitting particles with a vacuum aerodynamic diameter between 50 and 1000 nm with a reasonable efficiency (P. S. K. Liu et al. 2007).

Martikainen et al. (2021) developed the concept of a soot particle agglomeration inlet (SPAI) and measured particles with an aerodynamic diameter of some nanometers with the AMS. SPAI grows the sampled particles by colliding them with particles of a sufficient size for passing the AMS inlet (Martikainen et al. 2021).

The aim of this thesis is to develop an inlet system for the AMS based on the principle introduced by Martikainen et al. (2021). The inlet system should improve the AMS detection range to particles below 50 nm. The inlet system should be field-deployable and applicable to many emission sources.

Chapter 2 focuses on aerosol sources, size classifications and particle growth processes. Chapter 3 introduces methods for generating sample aerosol and instrumentation for its characterization. Chapter 4 presents techniques for chemical composition analysis including the AMS. Chapter 5 shows the process for developing the agglomeration inlet including detailed explanations for experiments that can be duplicated for future scenarios. Results from calibration measurements and future developments are also discussed.

2. BACKGROUND

The aerosol size range has multiple definitions according to different sources, but a typical definition is from some nanometers to around 100 μm in aerodynamic diameter (Hinds 1999; Kulkarni et al. 2011.) Particles smaller than some nanometers are considered gas molecules or clusters of molecules and particles larger than 100 μm experience the effects of gravity more severely, and for example have a much higher terminal settling velocity (Hinds 1999). Sampling over this large of a size range is not possible using a single instrument and one has to consider which methods are suitable for measurement of aerosol from different sources (Kulkarni et al. 2011).

Knowledge of particle growth processes is crucial in understanding how they evolve in the atmosphere and how these processes can be used with instrument development. This chapter focuses on background material on aerosol sources and growth processes.

2.1 Aerosol sources and size classification

Particle diameter is typically the most important metric affecting a particle's properties (Hinds 1999). Size classifications are used for quick interpretations from only a few metrics. Aerosol emissions rarely consist of particles with a uniform size, known as monodisperse aerosol, creating a need for interpreting the entire aerosol. Size distributions are the tool most often used.

2.1.1 Size distributions

The following introduction to aerosol size distributions follows Hinds (1999). Aerosol measurements can often result in particle numbers distributed across different size bins with equal or differing intervals. If the intervals differ, it is difficult to compare the counts in each bin, since a bin with double the width of another would have more particles collected if all particle sizes had the same number of particles. A diagram, where the heights of different bins are comparable can be created by dividing the counts in all bins by their width.

In aerosol science, normalized distributions are often presented on a logarithmic scale due to most aerosol size distributions approximately fitting the log-normal distribution. There is no theoretical reason for this, but experiments have shown a good correlation for

many cases. The log-normal distribution is

$$df = \frac{1}{\sqrt{2\pi}d_p\ln\sigma_g} \cdot \exp\left(-\frac{(\ln d_p - \ln \text{CMD})^2}{2(\ln\sigma_g)^2}\right) dd_p, \quad (2.1)$$

where df is the fraction of particles with diameters between d_p and $d_p + dd_p$, σ_g is the geometric standard deviation (GSD) and CMD is the count median diameter which corresponds to the geometric mean diameter (d_g) of the log-normal distribution.

Sometimes, the point of interest is something other than the number size distribution. Surface area, volume and mass distributions are common in aerosol science. The surface area or the volume of a particle can be easily calculated if the particle is assumed to be spherical and the mass can be calculated from the volume if the density is known.

Surface and mass median diameters and diameters of average surface area or mass can be calculated from Hatch-Choate equations, if the count median diameter and geometric standard deviation of the distribution are known.

$$d_A = \text{CMD} \cdot \exp(b\ln^2\sigma_g), \quad (2.2)$$

where d_A is the desired diameter and b is a constant depending on the conversion. Values for b can be found e.g. in Hinds (1999, p. 102).

It is important to understand the difference of number, surface area and mass size distributions. Figure 2.1 shows an example of how these distributions and diameters compare. The number size distribution is weighed equally, the surface area distribution is weighed slightly to large particles and the volume or mass distributions are heavily weighed to large particles.

2.1.2 Size ranges

Size ranges can be used for simplifying aerosol distributions. Figure 2.2 illustrates the most important aerosol size ranges. PM_1 , $\text{PM}_{2.5}$ and PM_{10} correspond to particles with an aerodynamic diameter of 1, 2.5 or 10 μm or less, respectively. Coarse particles are defined as particles between $\text{PM}_{2.5}$ and PM_{10} . (Hinds 1999) World Health Organization (2021) have published recommendations for $\text{PM}_{2.5}$ and PM_{10} concentrations. $\text{PM}_{2.5}$ concentrations have been linked to illnesses and WHO (2021) have estimated that around 7 million annual premature deaths are linked to air pollution.

Ultrafine particles (UFPs) are defined as particles with a diameter between 1 and 100 nm (Hinds 1999). Schraufnagel (2020) points out that UFPs potential to cause harm to health is great, but the role they play in many illnesses is still unknown. WHO (2021) have not

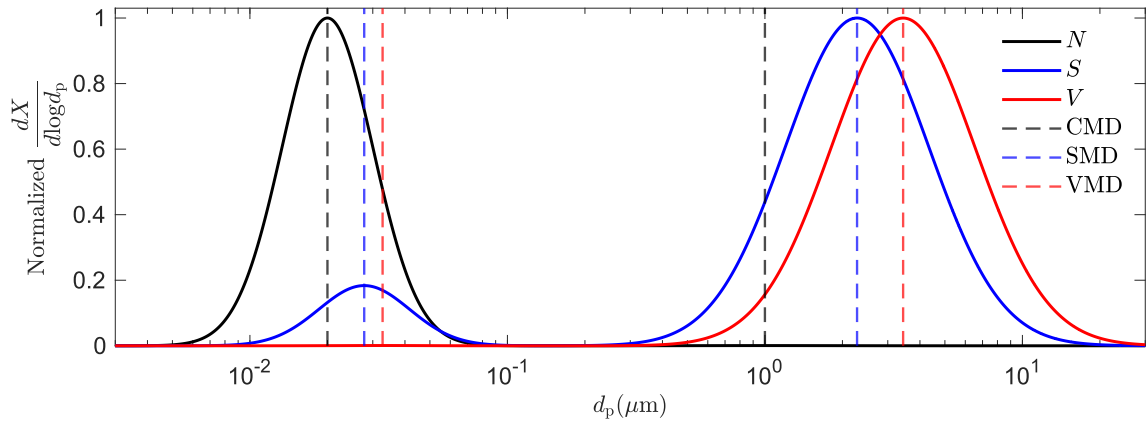


Figure 2.1. Example of a bimodal size distribution with $\text{CMD}_1 = 20\text{nm}$, $\text{CMD}_2 = 1.0\mu\text{m}$, $\sigma_{g,1} = 1.5$ and $\sigma_{g,2} = 1.9$. The particle number is 1000 times larger in the first peak. Normalized distributions of particle number (N), surface area (S) and volume (V) are presented with median diameters for each mode.

given recommendations for UFP concentrations due to insufficient evidence of the health effects. They have however introduced UFPs in their good practice statements that are meant to guide national and regional authorities.

The definition of nanoparticles is not as well established. Schraufnagel (2020) and Kulkarni et al. (2011) define nanoparticles the same way that UFPs have been defined (1–100 nm), while Hinds (1999) defines nanoparticles as particles with a diameter of less than 50 nm. For the purposes of this thesis, nanoparticles are defined as particles with an aerodynamic diameter below 50 nm to differentiate them from UFPs and to have a separate definition for particles below 50 nm.

Aerosol physics has different laws for the motion of particles with different sizes. Small particles interact with gas molecules as individual collisions while large particles see gas molecules as a constant fluid. The smallest particles are considered to be in the free molecular region and the larger particles in the continuum region. The particles inbetween are in the transition region. (Hinds 1999) These regions are also presented at standard pressure and temperature in Figure 2.2.

2.1.3 Aerosol sources

Often, aerosol are split into two categories according to their origin. Primary aerosol are directly emitted as particles while secondary aerosol are formed in the atmosphere from the gas phase by chemical reactions (Kulkarni et al. 2011; Seinfeld and Pandis 2016). Aerosol size distributions often consist of different modes. Kulmala et al. (2004) define particles in the of 3–20 nm size range as the nucleation mode, 20–90 nm as Aitken nuclei and 90–1000 nm as the accumulation mode.

The particles in different modes originate from different sources or processes. Vu et al.

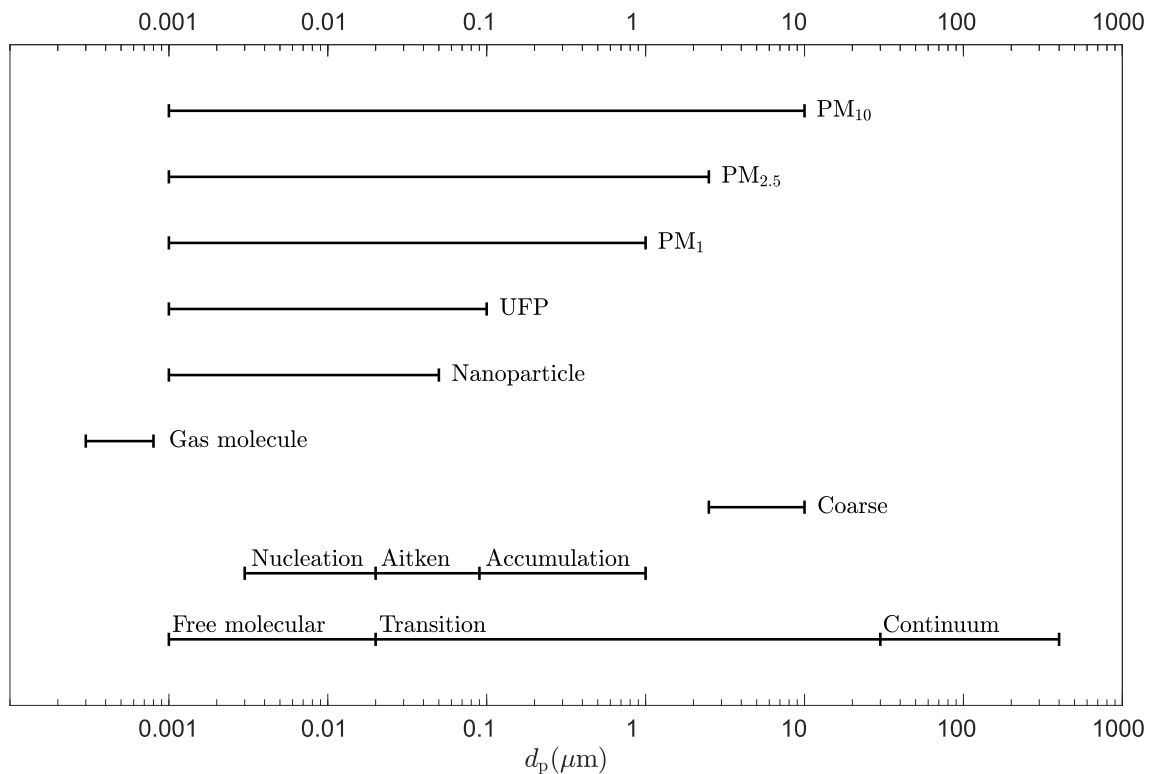


Figure 2.2. Aerosol size ranges, modified from Hinds (1999). Free molecular, transition and continuum regime are calculated at standard temperature and pressure.

(2015) mention that nucleation mode particles can originate from new-particle formation of emissions. New-particle formation will be discussed in section 3.1.2. Accumulation mode particles mainly originate from combustion or particle growth and coarse particles are typically created by mechanical processes (Vu et al. 2015). In addition to anthropogenic sources, natural processes can form particles in several size ranges (Seinfeld and Pandis 2016).

There are numerous sources of atmospheric aerosol, which all can not be covered in this thesis. Some major sources of coarse particles include salt aerosol generated from sea spray or de-icing salt on the roads, road dust resuspension, where dust deposited on roads is reintroduced to the atmosphere and non-exhaust emissions, including brake wear and tyre-road abrasion. It is important to note that most of these sources also emit particles below 2.5 μm with different formation mechanisms. (Matthaios et al. 2022)

Traffic is a major source of particle emissions. Vu et al. (2015) have reviewed many publications and determined that engine exhaust particles form a bimodal distribution. The first mode consists of nucleation mode particles below 30 nm in diameter that are believed to be formed by nucleation of sulfuric acid. The second mode is made of mostly soot particles in the size range of 30 to 500 nm. (Vu et al. 2015)

Other combustion sources also play a major role in the emissions of nanoparticles. Vu et al. (2015) have reviewed multiple articles agreeing that coal, oil and biomass combustion

generate particles in the UFP size range. Other sources of nanoparticles include cooking with a typical particle size of 20–70 nm and brake wear which produces very small nucleation mode particles in addition to the larger particles discussed before (Vu et al. 2015).

In addition to primary aerosol directly emitted from local emission sources, a major factor can be long range transport aerosol. As small primary particles are transported in the atmosphere, they interact with each other and with secondary aerosol and usually grow to the accumulation mode size range. The mechanisms affecting particle growth are discussed in section 2.2, but the main reason for why particles are transferred to the accumulation mode and not the coarse mode is due to coagulation (see 2.2.1) slowing down for larger particles. (Seinfeld and Pandis 2016)

The last important source of atmospheric aerosol discussed in this section is secondary aerosol. Secondary aerosol is often formed by oxidation of different gaseous compounds. Secondary organic aerosol (SOA) are formed by oxidation of volatile organic compounds (VOCs) which condense on each other or already existing particles. (Seinfeld and Pandis 2016) Sbai et al. (2021) have measured secondary aerosol from different sources using an oxidation flow reactor (OFR) and found that SOA particles are very small, usually around 20 nm in diameter. The size range of atmospheric SOA is not as easily defined, due to the contribution of many particle growth processes in the atmosphere.

2.2 Particle growth

Particle growth is an important aspect of this thesis and knowledge about it is required with understanding the instrument developed in this thesis. There are two main ways for achieving particle growth of already existing particles, coagulation and condensation. Coagulation means that particles adhere to each other, growing in size, and condensation means the transfer of vapor onto the particle surface. (Hinds 1999; Friedlander 2000)

2.2.1 Coagulation

When an aerosol particle hits a surface, it is most likely going to attach firmly. This is one of the key characteristics distinguishing aerosol particles from gas molecules and macroscopic particles. The forces causing this adhesion include the van der Waals force, the electrostatic force and forces linked to surface tension of absorbed liquids. These adhesion forces are very strong and adhered particles can be difficult to remove. (Hinds 1999) Particle bounce can occur if the velocity between a particle and a surface is great. Although possible, particle bounce is discluded from the consideration of coagulation and two particles are thought to adhere if they collide. (Friedlander 2000)

Coagulation can occur due to the Brownian motion of particles, which is called thermal

coagulation. If an external force, such as electricity affects coagulation, it is called kinetic coagulation. The simplest case of coagulation is that of monodisperse spherical particles with a diameter above 100 nm, where the two adhering particles form a new sphere. It is called Smoluchowski coagulation. (Hinds 1999)

The following theory is based on Hinds (1999). Fick's first law of diffusion gives the particle flux J at the surface of a selected particle

$$J = -D \frac{dN}{dx}, \quad (2.3)$$

where N is the number concentration, $\frac{dN}{dx}$ is the concentration gradient and D is the diffusion coefficient of particles

$$D = kTB, \quad (2.4)$$

where k is the Boltzmann constant, T is temperature and B is the particle's mechanical mobility. The rate of collisions between a select particle and other particles can be calculated by multiplying the particle flux with the area of the collision surface A_s which is the area of a sphere with a diameter twice that of a single particle ($d_s = 2d_p$). The rate of collisions ($\frac{dn}{dt}$) is

$$\frac{dn}{dt} = A_s J = -\pi(2d_p)^2 D \frac{dN}{dx}. \quad (2.5)$$

The concentration gradient at the collision surface is

$$\frac{dN}{dx} = -2 \frac{N}{d_p} \quad (d_p > \lambda_p), \quad (2.6)$$

where λ_p is the mean free path of the particle. Now, the rate of collisions becomes

$$\frac{dn}{dt} = 8\pi d_p D N. \quad (2.7)$$

Due to all particles being identical, this is the rate for every particle. The rate of collisions per unit volume of aerosol ($\frac{dn_c}{dt}$) is just the rate multiplied by N . A factor of 1/2 is applied to avoid counting the collisions twice

$$\frac{dn_c}{dt} = 4\pi d_p D N^2. \quad (2.8)$$

Each collision reduces the number of particles by one meaning that the rate of collisions

is equal to the rate of change in number concentration, just with an opposite sign

$$\frac{dN}{dt} = -4\pi d_p D N^2. \quad (2.9)$$

The coagulation coefficient for particles larger than 100 nm K_0 is defined as

$$K_0 \equiv 4\pi d_p D = \frac{4kTC_c}{3\mu}, \quad (2.10)$$

where C_c is the Cunningham slip correction factor defined by equation 2.11 and μ is the dynamic viscosity of the fluid.

$$C_c = 1 + \frac{\lambda}{d_p} \left[2.34 + 1.05 \cdot \exp \left(-0.39 \frac{d_p}{\lambda} \right) \right], \quad (2.11)$$

Equation 2.9 can now be reduced to

$$\frac{dN}{dt} = -K_0 N^2. \quad (2.12)$$

A correction for nanoparticles is required as the coagulation coefficient is only determined for particles larger than 100 nm. The correction is done by multiplying the coagulation coefficient with the Fuchs correction factor β_F ($K = K_0 \beta_F$). There are multiple definitions for this correction factor and Seinfeld and Pandis (2016) have collected the factors from five different sources. Fuchs and Sutugin (1971), as cited by Seinfeld and Pandis (2016) define the correction factor as

$$\beta_F = \frac{1 + \text{Kn}}{1 + 1.71\text{Kn} + 1.33\text{Kn}^2}, \quad (2.13)$$

where Kn is the Knudsen number

$$\text{Kn} = \frac{2\lambda}{d_p}, \quad (2.14)$$

where λ is the mean free path of the gas.

The particle number concentration in time $N(t)$ can be calculated from equation 2.12

$$N(t) = \frac{N_0}{1 + N_0 K t} \quad (2.15)$$

The maximum number of particles after time t limited by coagulation can be calculated from equation 2.15 by setting the starting concentration to infinity ($N_0 = \infty$) (Hinds 1999)

$$N(t) = \frac{1}{Kt}. \quad (2.16)$$

Equation 2.12 shows that the rate of change in number concentration is proportional to N^2 , which means that a highly concentrated aerosol coagulates more rapidly. The rate of change is also proportional to the coagulation coefficient, which is proportional to the Cunningham slip factor which is larger for small particles. This means that an aerosol with a small particle diameter and a high concentration will coagulate fastest.

The following theory only covers monodisperse particles, but in reality nearly all aerosols are polydisperse. The coagulation of an aerosol consisting of particles with two distinct diameters can be calculated from equation 2.12 by changing the coagulation coefficient to

$$K_{1,2} = \pi(d_1D_1 + d_1D_2 + d_2D_1 + d_2D_2), \quad (2.17)$$

where d_i are the particle diameters and D_i are the particle diffusion coefficients (Hinds 1999).

Particle distributions are usually distributed into more than two particle diameters which requires another kind of calculation. Hinds (1999) proposes a calculation method for the average coagulation coefficient \overline{K} of a polydisperse aerosol split into discrete size intervals

$$\overline{K} = \sum_{i=1}^k \sum_{j=1}^k K_{ij} f_i f_j, \quad (2.18)$$

where K_{ij} is the coagulation coefficient for a polydisperse aerosol with two distinct diameters calculated from equation 2.17 and f_i and f_j are the fractions of the total number of particles in the two distinct size intervals.

Equation 2.15 can be applied with \overline{K} for a time period where \overline{K} does not change appreciably. If one is to calculate the concentration of a polydisperse aerosol in time, \overline{K} has to be calculated periodically for the new distribution. The calculation of \overline{K} is very consuming and is done with computer programs. Analytical solutions exist for log-normally distributed aerosols. (Hinds 1999)

This analysis was constrained by the assumption that two colliding particles form a new spherical particle. In reality, particles often attach on each other and form agglomerates. An agglomerate consists of primary particles and the number of primary particles is related to a characteristic radius with fractal dimension (D_f) in the exponent. These fractal dimensions are used when analyzing agglomerated particles. (Friedlander 2000)

To study how particles either stick together and form agglomerates or coalesce in to a

single spherical particle can be done using characteristic times for collisions and coalescence. If the characteristic time for coalescence is much smaller than that of collisions, the formed particles will be spherical, if it is the opposite way, the formed particles will be agglomerates. If the characteristic times are in a similar scale, aggregates can be formed, where individual particles can be distinguished, but they have somewhat coalesced together. (Friedlander 2000)

Apart from naturally occurring Brownian coagulation, kinematic coagulation can be used to increase the collision frequency between particles. For example, when coagulation is caused by a flow in a system, which is often called shear coagulation. Shear coagulation is important in turbulent flows. (Friedlander 2000) Acoustic coagulation is used when particles of different sizes oscillate at different amplitudes. The oscillations are caused by high-energy sound waves. (Hinds 1999) Hautanen et al. (1995) designed a system for testing how electrical effects could increase coagulation. They noted that their experiments resulted in only a small reduction in particle concentration.

2.2.2 Condensation

Another way of achieving particle growth is condensation of gas phase vapor. Condensation is often favorable on already existing particles and can be achieved through multiple routes. (Friedlander 2000)

When looking at a system with liquid and vapor of the same substance, the saturation vapor pressure p_s can be calculated for ideal gasses using the Clapeyron equation

$$\frac{dp_s}{dT} = \frac{\Delta H p_s}{RT^2}, \quad (2.19)$$

where ΔH is the molar heat of vaporization and $R = 8.314 \frac{\text{J}}{\text{K}\cdot\text{mol}}$ is the gas constant (Friedlander 2000). The saturation ratio S_R is defined as the ratio between the partial pressure of vapor and the saturation vapor pressure of that same vapor in a system (Hinds 1999)

$$S_R = \frac{p}{p_s}. \quad (2.20)$$

The saturation ratio is often referred to as relative humidity (RH). The difference between these two is a multiplier of 100. Supersaturation is the portion of the saturation ratio that is larger than one, for example a saturation ratio of 1.03 corresponds to a supersaturation of 3%. (Hinds 1999)

Supersaturation can be achieved for example by adiabatic expansion or mixing (Friedlander 2000). An adiabatic expansion does not require heat from the surroundings and is

often achieved by rapid expansion of a gas (Hinds 1999). The adiabatic process for an ideal gas can be expressed as

$$\frac{p_2}{p_1} = \left(\frac{T_2}{T_1} \right)^{\frac{\gamma}{\gamma-1}}, \quad (2.21)$$

where γ is the ratio of the specific heat capacities at constant pressure compared to constant volume (Friedlander 2000). Equation 2.21 shows that an adiabatic expansion, which is equivalent to the decrease of pressure leads to a decreased temperature, as $\gamma > 1$.

The saturation vapor pressure is defined for flat surfaces. If the surface is curved, for example, a spherical particle, the saturation vapor pressure will be greater. This is called the Kelvin effect and the saturation ratio can be calculated using the Kelvin equation

$$\frac{p_d}{p_s} = \exp \left(\frac{4\sigma M}{\rho R T d_p^*} \right), \quad (2.22)$$

where σ is the surface tension, M is the molar mass, ρ is the density of the liquid droplet and d_p^* is the Kelvin diameter, the diameter of a particle in equilibrium with partial pressure p_d . (Hinds 1999)

The Kelvin equation applies only for pure liquids. The vapor pressure of a solute differs from that of a pure liquid. The saturation ratio for solutions can be calculated

$$\frac{p_d}{p_s} = \exp \left(\frac{4\sigma \bar{v}_1}{d_p R T} - \frac{6n_2 \bar{v}_1}{\pi d_p^3} \right), \quad (2.23)$$

where \bar{v}_1 is the partial molar volume of the solvent and n_2 is the number of moles of solute. (Friedlander 2000) This equation can also be expressed as

$$\frac{p_d}{p_s} = \left(1 + \frac{6imM_w}{M_s \rho \pi d_p^3} \right)^{-1} \exp \left(\frac{4\sigma M_w}{\rho R T d_p} \right), \quad (2.24)$$

where i is the number of ions each salt molecule forms when it dissolves, m is the mass of the dissolved salt and M_w and M_s are the molecular weights of the solvent and salt, respectively (Hinds 1999). These equations are called the Köhler equations. For the equation by Friedlander (2000), the first term on the right corresponds to the Kelvin effect of the pure solvent and the other term corresponds to vapor pressure lowering of the solute. For the equation by Hinds (1999), these terms are reversed. These equations show, that the added salt is a major influence lowering the required saturation ratio of small droplets while having little influence on the larger particles that follow the Kelvin equation.

Condensation can generally take two routes. Homogenous nucleation is the process where particles are formed from supersaturated vapor without the assistance of condensation nuclei (Hinds 1999). Heterogenous supersaturation occurs when particles are present and condensation takes place on already existing nuclei (Friedlander 2000).

The theoretical saturation ratios required for homogenous nucleation are very high, but experiments have shown that homogenous nucleation occurs at lower saturation ratios. This can be explained by the fact that individual molecules do not act as condensation nuclei, instead they form small clusters which act as condensation nuclei if they reach a sufficient size. (Hinds 1999)

Heterogenous condensation requires a much lower supersaturation typically just a few percent if the particle concentration is high. Cloud droplet formation often takes place when warm air rises, cools down and condenses on already existing atmospheric particles. (Friedlander 2000)

The rate of condensation can be calculated for particles in different size ranges. The following rates are presented by Friedlander (2000). For large particles in the continuum regime ($K_n \gg 1$), the volumetric growth rate can be expressed as

$$\frac{dv}{dt} = \frac{2\pi D d_p v_m}{kT} (p_1 - p_d), \quad (2.25)$$

where v_m is the molecular volume of the condensing species and p_1 is the partial pressure of vapor far away from the particle surface. For small particles in the free molecular regime ($K_n \ll 1$), the following equation is used

$$\frac{dv}{dt} = \frac{\alpha \pi d_p^2 v_m (p_1 - p_d)}{\sqrt{2\pi m k T}}, \quad (2.26)$$

where α is the accommodation coefficient, usually $\alpha = 1$. For the transition regime ($K_n \approx 1$), the Fuchs correction factor β_F can be used for correcting the continuum regime equation.

The condensation particle counters discussed in section 3.2 utilize condensation by supersaturation in the transition between a heated and a cooled region.

3. INSTRUMENT CALIBRATION

Development of aerosol instrumentation relies on generating aerosol particles with known characteristics. This chapter focuses on particle generation and analysis methods that can be used in instrument calibration.

3.1 Particle generation

Particle generation is an important aspect for example in generating a desired test aerosol or with instrument calibration (Hinds 1999). Multiple ways of generating test aerosol exist, but atomizers and tube furnaces will be addressed in this section as they are methods required in the thesis.

3.1.1 Atomizers

Lefebvre and McDonell (2017) define atomizers as devices used to create sprays. Many different types of atomizers exist, but they all share the same principle of creating a high relative velocity between a liquid and a surrounding gas (Lefebvre and McDonell 2017).

The most basic type of atomizer is a pressure atomizer with a plain orifice, where liquid is discharged from a small aperture with high pressure. Other types of atomizers include rotary atomizers, which achieve atomization by rotating a disk with liquid in its center. Electrostatic or ultrasonic atomizers can also be used in some applications. (Lefebvre and McDonell 2017)

There are three main ways of droplet deformation depending on the flow pattern around them. Hinze (1955) has illustrated and explained these patterns but the main idea is that a drop in an airstream deforms and creates smaller droplets of different sizes (Hinze 1955). The middle part of the droplet is in charge of generating the smallest particles, while the rim which also contains most of the mass generates larger droplets (Lefebvre and McDonell 2017).

Most atomizers used for generation of submicron particles generally utilize the same principle of having compressed air drag fluid from a reservoir using the Bernoulli effect. The liquid is then directed onto a surface to remove the largest particles and return them to the reservoir. (Hinds 1999) These atomizers are called collision atomizers (May 1973). An

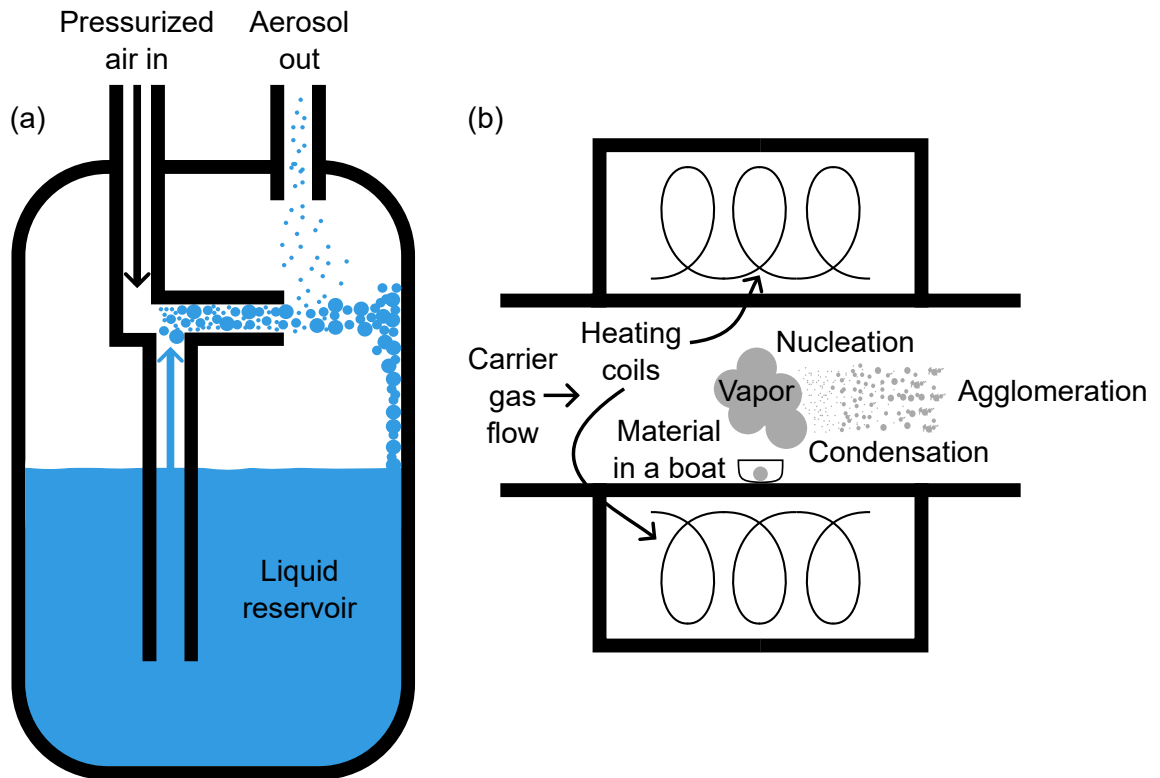


Figure 3.1. (a) Atomizer based on May (1973) and Topas GmbH (2024) and (b) particle formation in a tubular furnace based on Scheibel and Porstendörfer (1983) and Backman et al. (2002).

illustration of a collision atomizer is provided in Figure 3.1 (a). A common disadvantage with this design is that the solvent is evaporated from the system making the liquid more concentrated and changing the dynamics of the output aerosol (B. Y. Liu and Lee 1975).

May (1973) proposed that a larger liquid container could be used to make the effect smaller and B. Y. Liu and Lee (1975) solved the problem of the changing concentration by inputting the liquid with constant flow using a syringe. Despite this technology, many commercial atomizers do not use the syringe technique. For example, the TSI model 3076 aerosol generator (TSI Inc. 2024) and Topas model 220 aerosol generator (Topas GmbH 2024) are commercial atomizers using a liquid reservoir instead of a syringe pump. Both of these generators are capable of producing particles from dozens of nanometers to hundreds of nanometers in diameter (Topas GmbH 2024; TSI Inc. 2024).

The sampled aerosol needs to be dried to remove extra moisture. This can be done in multiple ways. Colbeck and Lazaridis (2014) present that drying can be achieved by membrane dryers, diffusion dryers, dilution or heating. The biggest disadvantage of the membrane dryer is that it requires purge air with a dew-point temperature of $-20\text{ }^{\circ}\text{C}$, which is difficult to achieve in remote locations. A diffusion drier is very cheap and does not require too labor intensive maintenance as the silica gel inside the drier needs to be replaced or changed only if the drier is saturated with water. Dilution has multiple

disadvantages, but if used, the dilution ratio has to be monitored closely. Drying by heating requires heating a long period of sampling line and is often unfeasible. (Colbeck and Lazaridis 2014)

3.1.2 Tube furnaces

Tube furnaces can be used for generation of a stable test aerosol. Tube furnaces which are also referred to as evaporation-condensation aerosol reactors can be used for achieving a very high concentration of very small nanoparticles with a relatively narrow size distribution (Scheibel and Porstendörfer 1983).

The particles generated in a tube furnace are formed by gas-to-particle conversion. The process starts with a vapor of the desired material that is produced in the heated furnace. (Scheibel and Porstendörfer 1983) The vapor then forms small nuclei and grows by condensation. The formed particles then coagulate and form agglomerates, aggregates or spheres. The final shape of the particles is dependent on which process dominates in which part of the system. (Ulrich 1971)

A typical furnace has a ceramic tube that does not evaporate at the operating temperatures of the furnace. The material for the particles is kept in a boat that is also made of a non-evaporating material. The material is transported to the end of the furnace by a carrier gas. (Scheibel and Porstendörfer 1983) A schematic of particle formation in a tube furnace is presented in Figure 3.1 (b).

Particle formation can be modified by many methods. Cooling and dilution cause the primary particle size to remain small making the formed particles agglomerates. If the cooling is slow, particles will coalesce or sinter together and form large primary particles which coagulate slowly. (Backman et al. 2002) Scheibel and Porstendörfer (1983) state that cooling can also be achieved by varying the flow rate going through the furnace. The amount of vapor present affects the particle size. The varying vapor levels can be achieved by changing the temperature of the furnace or by changing the position of the boat. If the temperature is raised or the boat is moved to the beginning of the furnace, the particle size will be larger as the vapor has more time to condense into larger particles. (Scheibel and Porstendörfer 1983)

Tube furnaces can produce particles from a variety of materials. The process is only limited by the material of the boat and the tube. For example, Scheibel and Porstendörfer (1983) have produced Ag and NaCl nanoparticles, Magnusson et al. (1999) have produced Au nanoparticles and Kruis et al. (2000) have produced PbS nanoparticles. This variability and known characteristics of particles produced by furnaces make it a suitable tool for generating nanoparticles for instrument validation.

3.2 Scanning mobility particle sizer (SMPS)

Particle number size distributions can be measured by combining two different instruments, namely the differential mobility analyzer (DMA, Knutson and Whitby 1975) and the condensation particle counter (CPC, Agarwal and Sem 1980). S. C. Wang and Flagan (1990) introduced the combination of these two instruments for this purpose and called it the scanning electrical mobility spectrometer (SEMS). This principle was commercialized by TSI Inc. and the instrument is more commonly referred to as the scanning mobility particle sizer (SMPS) (Kulkarni et al. 2011).

The following theory is presented according to Hinds (1999). A moving particle experiences a drag force (F_D) that is calculated using Stoke's law when $Re < 1$, or in the so called Stoke's regime

$$F_D = \frac{3\pi\mu V d_p}{C_c}, \quad (3.1)$$

where μ is the dynamic viscosity of the fluid, V is the velocity of the particle, d_p is particle diameter and C_c is the Cunningham slip correction factor. The Reynolds number for a particle can be calculated from

$$Re = \frac{\rho_g V d_p}{\mu}, \quad (3.2)$$

The terminal electrostatic velocity of a charged particle in an electrical field can be calculated by assuming that the drag force is equal to the electrostatic force experienced in the electrical field $F_E = neE$, where n is the number of elementary charges, e is the charge of an electron ($1.6 \cdot 10^{-19}C$) and E is the electrical field strength.

The settling velocity can be calculated from these equations and it is

$$V_{TE} = \frac{neEC_c}{3\pi\mu d_p}. \quad (3.3)$$

The relation between electrostatic terminal settling velocity and electrical field strength is often expressed as electrical mobility (Z)

$$Z = \frac{V_{TE}}{E}. \quad (3.4)$$

This definition for V_{TE} is applicable only in the Stokes regime ($Re < 1$).

The simplest electrical mobility analyzer consists of two plates with opposing charges. All particles with a mobility up to a certain point will pass through and all particles with a

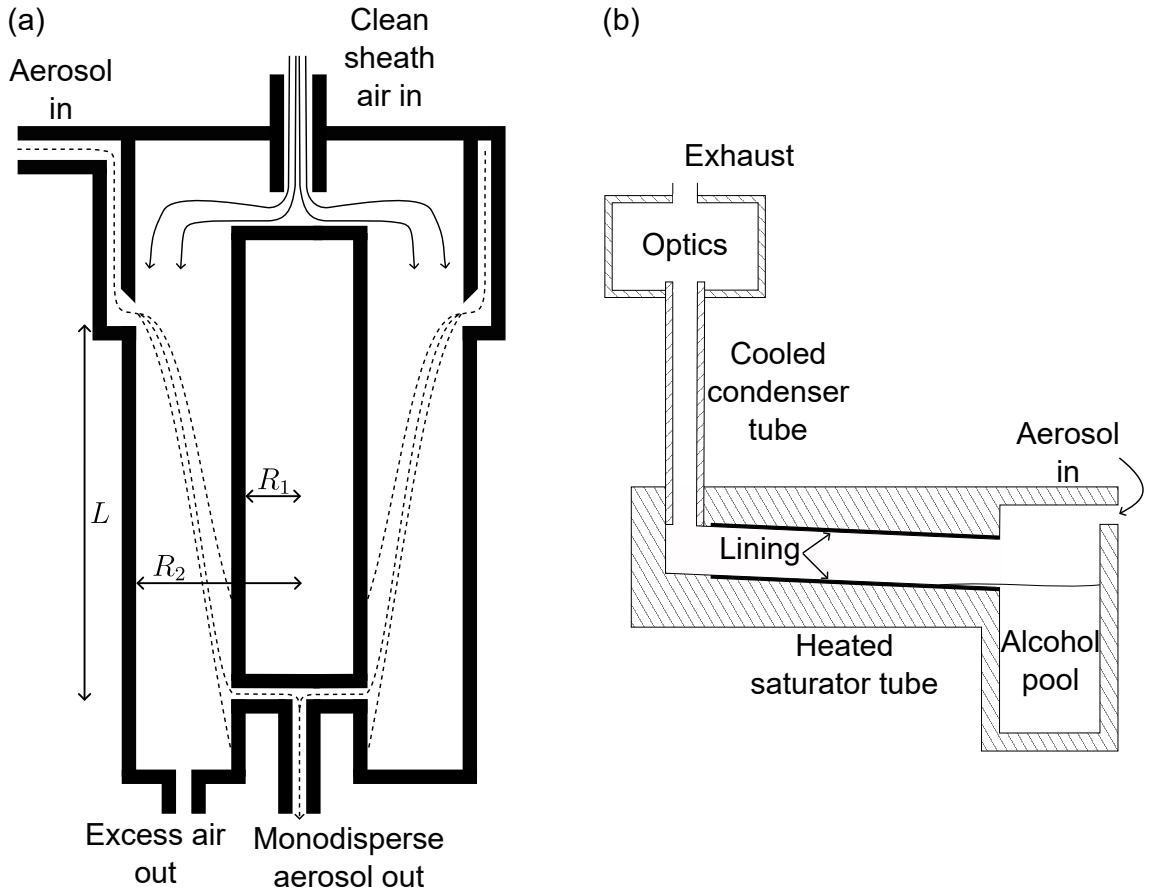


Figure 3.2. (a) A schematic of the DMA based on Knutson and Whitby (1975) and (b) the CPC based on Agarwal and Sem (1980).

higher mobility will be caught on the plates. (Hinds 1999) The DMA uses a more sophisticated configuration with the same working principle.

The DMA is illustrated in Figure 3.2 (a). The aerosol enters the DMA through a narrow opening in the outer electrode while particle-free sheath air enters the DMA through the top of the cylinder. The aerosol sample is extracted from the bottom of the inner electrode and excess air is removed from the bottom of the cylinder. Only particles with a mobility in a narrow range are extracted and particles with low mobilities are deposited downstream the opening or discharged with the excess flow. Particles with high mobilities are collected on the central electrode. (Kulkarni et al. 2011)

The electrical field in a standard cylindrical DMA is

$$E = \frac{V}{r \ln \frac{R_2}{R_1}}, \quad (3.5)$$

where V is the potential applied to the inner electrode, r is radius and R_1 and R_2 are the radii of the inner and outer electrodes, respectively, seen in Figure 3.2 (a) (Kulkarni et al. 2011). The characteristic mobility Z^* of particles classified at known flow rates and

applied voltage, can be derived from the definition of the electrical field and it is

$$Z^* = \frac{(Q_{sh} + Q_e) \ln \frac{R_2}{R_1}}{4\pi V L}, \quad (3.6)$$

where Q_{sh} is the sheath flow, Q_e is the exhaust flow and L is length between the aerosol entrance to the DMA and the aerosol exit from the DMA (Kulkarni et al. 2011).

The calculation of the particle mobility in an electrical field requires information about the particle charge. The aerosol entering the DMA is neutralized using a bipolar charger that generates a known charge distribution (Kulkarni et al. 2011). Several methods exist for calculating this charge distribution. The simplest way of calculating the charge distribution is by assuming that continuously bipolarly charged particles end up in an equilibrium described by the Boltzmann distribution (Kulkarni et al. 2011). This only applies for equilibrium and not stationary states, which caused Fuchs (1963) to develop a method for calculating the charge distribution from the rate of ion diffusion to particles with differing charges.

Fuchs (1963) made an error in his derivation and Hoppel and Frick (1986) later corrected this theory to include three body trapping. Each of these theories better predicted the experimental results but they are all quite complex to calculate. Wiedensohler (1988) created an approximation for calculating the charge distribution in the size range of 1–1000 nm for a single charge and 20–1000 nm for two charges. The fraction of certain charges $f(N)$ can be calculated

$$f(N) = 10^{\left[\sum_{i=0}^5 a_i(N) \cdot \left(\log \frac{d_p}{nm} \right) \right]}, \quad (3.7)$$

where $a_i(N)$ are approximation coefficients listed in Wiedensohler (1988), N is the number of charges and d_p is the particle diameter in nanometers. The approximation coefficients have since been updated and the correct values can be found from e.g. Kulkarni et al. (2011, p. 352)

The neutralizers have been typically based on ion generation caused by radioactive decay. Many isotopes have been used, but TSI have commercialized a ^{85}Kr neutralizer (TSI 3077). TSI have also created a soft x-ray neutralizer (TSI 3088) which is often used with newer SMPS instruments.

The DMA is used to create a monodisperse aerosol, but by combining it with a particle counter, a particle size distribution can be obtained by stepping or continuously scanning the voltage (Hinds 1999). If the voltage is changed in steps, the instrument is called the differential mobility particle sizer (DMPS) and with continuous voltage variation, the device is called the scanning mobility particle sizer (SMPS) (Kulkarni et al. 2011). S. C.

Wang and Flagan (1990) expressed that the entire size distribution could be gathered in a few minutes which would allow for study of aerosol undergoing relatively rapid changes.

The detector used for counting the particles after the DMA is the condensation particle counter (CPC). The working principle for detecting atmospheric dust particles was discovered already in the 19th century by Aitken (1888). The principle that Aitken (1888) used included supersaturating the air and growing the particles by condensation and counting the particles using a magnifying glass. The condensation nucleus counter (CNC) described by Agarwal and Sem (1980) shared this idea of particle growth by condensation and optical detection, albeit with a more sophisticated system. The instrument described by Agarwal and Sem (1980) will be referred to as a CPC from this point on due to it being the most common term used.

The schematic of a condensation particle counter is shown in Figure 3.2 (b). The details about particle growth by condensation are given in subsection 2.2.2. Many different types of CPCs exist for different purposes (Kulkarni et al. 2011), but the following description of the CPC is based on a conductive cooling CPC described by Agarwal and Sem (1980) as it is commonly used in SMPS systems (Kulkarni et al. 2011). The aerosol enters the instrument through an inlet and is brought to the saturator, which is a tube with a lining partially dipped into a butanol reservoir located at the inlet of the saturator. The temperature of the saturator is controlled by an electrical resistance heater.

The saturated aerosol is then cooled in a condenser tube, where the temperature is controlled by a thermoelectric cooler. The butanol condenses on the particles in the condenser and the particles pass to the optics. The optics include a light source, a condensing lens, a narrow aperture slit and an imaging lens. After the optics, the aerosol passes through a filter and is removed by a pump.

The particles can be counted by two modes of operation. The count mode is used for lower concentrations and the limit depends on the instrument. In the count mode, single electrical pulses of individual particles are counted. The second mode of operation is the photometric mode. If the electrical signals of particles overlap too much, individual particles can no longer be counted. In this case, the detector is switched to the photometric mode, where the voltage level scattered by all particles in a viewing volume is measured.

The design by Agarwal and Sem (1980) was limited in its ability to detect the smallest particles, which caused Stolzenburg and McMurry (1991) to develop a CPC with a lower cutoff size. It was achieved by reducing diffusion losses at the inlet and with more accurate confinement of particles to the area with the highest supersaturation inside the condenser (Stolzenburg and McMurry 1991). CPCs can also detect smaller particles by changing the working fluid (Kulkarni et al. 2011).

4. CHEMICAL COMPOSITION ANALYSIS

The chemical composition of aerosol particles can be analyzed by many methods. This chapter focuses on the soot particle aerosol mass spectrometer (SP-AMS) as it is the main instrument of this thesis. Other chemical analysis methods will be visited along with a method for improving the detection range of the SP-AMS.

4.1 Soot particle aerosol mass spectrometer (SP-AMS)

The aerosol mass spectrometer (AMS, Aerodyne Inc., Jayne et al. 2000) was developed as a method for enabling real-time analysis of the composition, mass concentration and size distribution of atmospheric particles. The AMS has received numerous upgrades after its introduction and the instrument used in this thesis is based on the high-resolution time-of-flight aerosol mass spectrometer (HR-ToF-AMS) developed by DeCarlo et al. (2006). The AMS lacks the ability of detecting black carbon, due to its vaporization method. Onasch et al. (2012) created a new vaporizer for detecting black carbon and other refractory species. The instrument including a soot particle (SP) module is called the soot particle aerosol mass spectrometer (SP-AMS), which is the main instrument in this thesis, depicted in Figure 4.1.

4.1.1 Aerodynamic lens

The invention enabling the advancement of the AMS is the aerodynamic lens (P. Liu et al. 1995a; P. Liu et al. 1995b). The main idea of an aerodynamic lens is to have multiple axisymmetric contractions and enlargements in series focusing particles in the stream to the center (P. Liu et al. 1995a).

The following theory is based on P. Liu et al. (1995a). A particle crossing a contraction and an expansion, or a so called aerodynamic lens is deviated from the fluid streamline due to inertial effects, illustrated in Figure 4.2. This means that the particle radial position $r_p(\infty)$ differs from the fluid streamline radial position $r_0(\infty)$. The deviation can be explained by the particle stream concentration factor η , defined as

$$\eta = \frac{r_p(\infty)}{r_0(\infty)}. \quad (4.1)$$

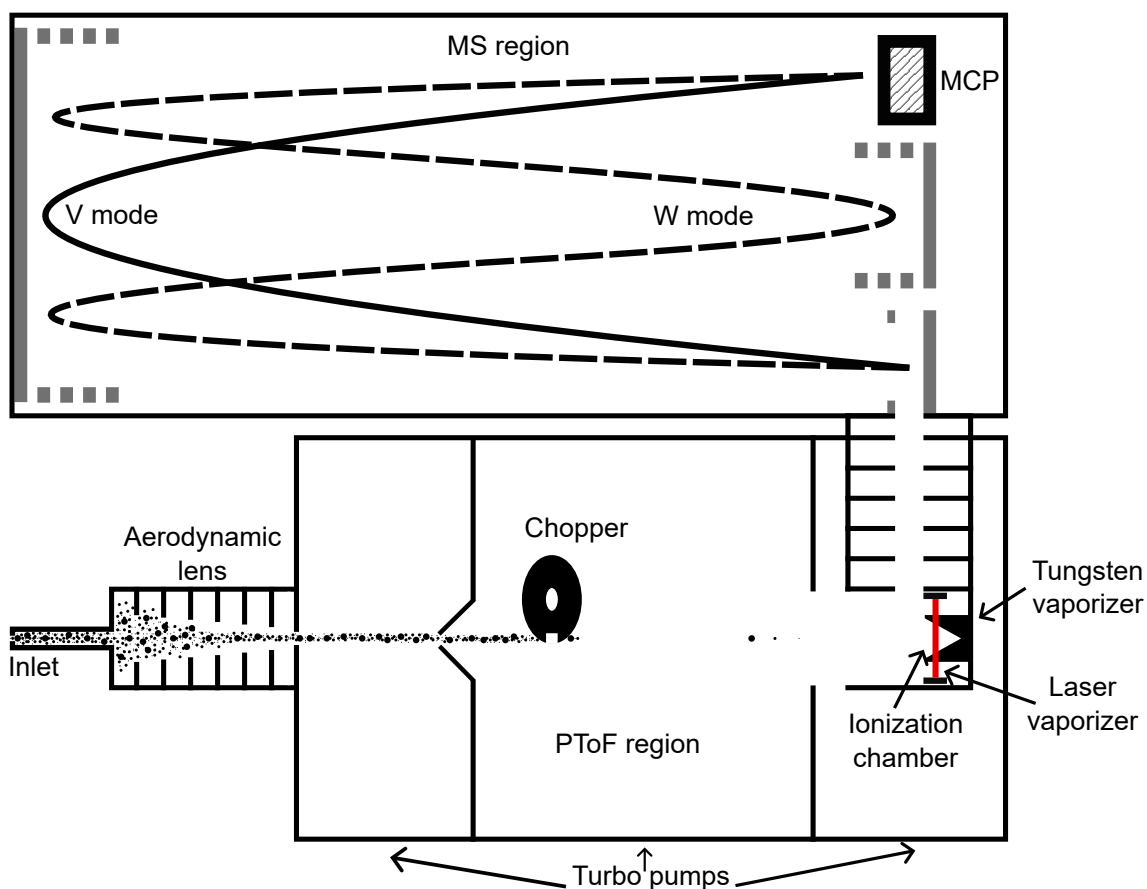


Figure 4.1. An illustration of the soot particle aerosol mass spectrometer. Adapted from DeCarlo et al. (2006) and modified by description of Onasch et al. (2012).

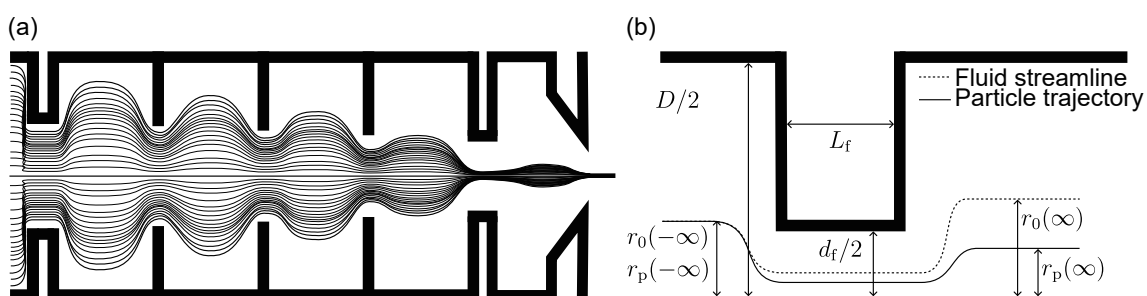


Figure 4.2. (a) An illustration of particle trajectories in the aerodynamic lens (Jayne et al. 2000) and (b) an illustration of particle and fluid trajectories in a single contraction (P. Liu et al. 1995a). L_f is the length of the contraction, $d_f/2$ is the radius of the contraction and $D/2$ is the radius before the contraction.

The concentration factor for particles in an incompressible isothermal flow is

$$\eta = 1 - \frac{3}{4}S \int_{-\infty}^{\infty} \frac{1}{\tilde{U}} \left(\frac{d\tilde{U}}{d\tilde{z}^2} d\tilde{z} \right), (S \rightarrow 0), \quad (4.2)$$

where S is the Stokes number defined by equation 4.3, $\tilde{U} = \frac{U}{U_0}$ and $\tilde{z} = z/L_0$, where U and U_0 are the flow velocity and characteristic flow velocity of the fluid, respectively, z is length and L_0 is characteristic length.

$$S = \frac{\tau_0 U_0}{L_0}, \quad (4.3)$$

where τ_0 is the particle relaxation time defined as

$$\tau_0 = \frac{\rho_p d_p^2 C_c}{18\mu}, \quad (4.4)$$

where ρ_p is the density of the particles, d_p is their aerodynamic diameter, and C_c is the Cunningham slip correction factor for correcting the slip effects of particles defined by equation 2.11. This correction has been changed from P. Liu et al. (1995a) to unify the variables used in this thesis and it is adapted from Hinds (1999). μ is the fluid dynamic viscosity.

Equation 4.2 applies for fluids where the particle relaxation time is constant. For isentropic flows of perfect gasses, the following equation applies

$$\eta = 1 - \frac{3}{4}S \int_{-\infty}^{\infty} \frac{1}{\tilde{T}^{\frac{1}{2}} \tilde{\rho}^3 \tilde{U}} \left[\frac{d(\tilde{\rho} \tilde{U})}{d\tilde{z}} \right]^2 \left\{ \frac{1 + \frac{1}{3}\gamma M^2}{1 - M^2} \right\} d\tilde{z}, (S \rightarrow 0), \quad (4.5)$$

where $\tilde{T} = T/T_0$ is the ratio of temperatures at the inlet and in the fluid, $\tilde{\rho} = \rho/\rho_0$ is the ratio of fluid densities at the inlet and in the fluid. M is the flow local Mach number and γ is the specific heat ratio.

It can be seen from equations 4.2 and 4.5 that the stream contraction factor η is always less than one in these two respective cases for small particles near the centerline of the flow. If η is between -1 and 1, particles will be concentrated on the central axis. If the Stokes number is large, η will be less than -1, and particles will be deviated from the centerline of the fluid due to inertial effects. This is the reason, why large particles are not efficient at lens transmission. (P. Liu et al. 1995a)

According to the aforementioned theory, the smallest particles will efficiently move to the centerline of the fluid. Diffusion caused by Brownian motion, and lift-force in a nozzle

expansion are reasons for the loss of nanoparticles in an aerodynamic lens. The following theories for these effects are presented according to P. Liu et al. (1995a).

During an expansion through a nozzle, the velocity distribution of thermal movement of particles can be approximately described using the Maxwell-Boltzmann distribution. The radial distribution of the particle beam at distance $z = L$ can be obtained from the Maxwell-Boltzmann distribution by assuming that the radial velocity does not change significantly after the expansion. The radial distribution of the particle beam as a function of radial distance (r) is

$$f(r)dr = \frac{1}{\pi a_B^2} \exp\left(-\frac{r^2}{a_B^2}\right) 2\pi r dr, \quad (4.6)$$

where

$$a_B = \sqrt{\frac{2kT_{PF}}{m_p}} \frac{L}{U_{p\infty}}, \quad (4.7)$$

where k is the Boltzmann constant, T_{PF} is the particle frozen temperature which refers to the temperature of the particles after expansion, m_p is the mass of a particle and $U_{p\infty}$ is the particle mean velocity in the vacuum, which can be calculated from

$$U_{p\infty} = \frac{U_g - U_1}{1 + (d_a/d^*)^b} + U_1, \quad (4.8)$$

where U_g and U_1 are gas velocity exiting the lens and gas velocity within the lens, respectively, d^* and b are constants acquired from calibrations (Allan et al. 2003).

Particle beam width (d_B) is defined as the diameter, where 90% of the total particle number is included and it can be calculated from equation 4.6

$$d_{B,Brown} = 3.04a_B. \quad (4.9)$$

P. Liu et al. (1995a) note that in order to evaluate this limit, T_{PF} is required, which can be estimated as the upstream temperature. Zhang et al. (2004) modelled the dynamics of a nozzle expansion in an aerodynamic lens and found that T_{PF} is equal or less than the upstream temperature meaning that using the upstream temperature is a good upper limit.

Although diffusion is not affected by the particle mass, the kinetic energy experienced by the particle is, which means that a nanoparticle with a high density could penetrate the aerodynamic lens.

The lift forces during nozzle accelerations for nonspherical particles can be estimated based on their geometries. P. Liu et al. (1995a) offer ways for calculating the forces for cylinders, disks, spheroids and cuboids, but other geometries can also be calculated. The lift-force limit is dependent on the particle shape and can be expressed as

$$d_{B,Lift} \sim \delta L, \quad (4.10)$$

where δ is a factor describing the deviation of the particle shape from e.g. a sphere.

In conclusion, large particles are lost in the aerodynamic lens due to inertial effects while small particles are lost due to diffusion or lift-forces due to an irregular shape.

P. Liu et al. (1995a) have numerically modelled this theory and proven that it works for various symmetries and for configurations with multiple contractions. P. Liu et al. (1995b) have developed an aerodynamic lens based on these simulations. The aerodynamic lens used in the AMS consists of six orifices going from a diameter of 5 mm at the entrance to a diameter of 3 mm at the exit. The inlet is kept at atmospheric pressure (10^5 Pa, 760 Torr). A critical orifice with a diameter of 100 μm causes the pressure to drop to approximately 173 Pa (1.3 Torr). (P. S. K. Liu et al. 2007) The pressure at the end of the aerodynamic lens is approximately 1.3 mPa (10^{-5} Torr) (Jayne et al. 2000). The aerodynamic lens of the AMS is illustrated in Figure 4.2. The flow through the inlet is approximately 1.4 cm^3/s (P. S. K. Liu et al. 2007).

P. S. K. Liu et al. (2007) have measured the particle transmission efficiency of the aerodynamic lens in the AMS to be sufficient for sampling atmospheric accumulation mode particles between 50 and 1000 nm in vacuum aerodynamic diameter. The transmission efficiency is significantly reduced at both ends of this range (P. S. K. Liu et al. 2007). Peck et al. (2016) have developed a different aerodynamic lens for the AMS, allowing particles up to 2.5 μm to be measured, while losing a fraction of the smaller particles, but no solution exists for the transmission of nanoparticles.

The vacuum aerodynamic diameter can be calculated according to the following equation

$$d_{va} = \frac{\rho_p}{\rho_0} d_m S, \quad (4.11)$$

where ρ_p is the density of the particle, $\rho_0 = 1.0\text{g}/\text{cm}^3$ is unit density, d_m is the mobility diameter and S is the Jayne shape factor (DeCarlo et al. 2004). The Jayne shape factor can be calculated from experiments, where a differential mobility analyzer (DMA) selects particles with a known d_m and the AMS measures d_{va} . The Jayne shape factor can be approximated for particles toward the continuum regime limit with

$$S \cong \frac{1}{\delta^3 \chi_v \chi_t} \quad (4.12)$$

and for the free molecular limit with

$$S \cong \frac{1}{\delta^3 \chi_v \chi_t^{1/2}}, \quad (4.13)$$

where δ is the internal void fraction of the particle, χ_v is the dynamic shape factor in the free molecular regime and χ_t is the dynamic shape factor in the transition regime. In the case where the particle doesn't have internal voids, S will become approximately $1/\chi^2$ in the free molecular regime and $1/\chi^{\frac{3}{2}}$ in the continuum regime. (DeCarlo et al. 2004) As can be seen from equation 4.11, if a particle is spherical, its Jayne shape factor will be one, and d_{va} will only be dependent on the particle density.

4.1.2 Time-of-flight region

The time-of-flight (ToF) region is directly after the particle beam exits the aerodynamic lens. The expanding air at the exit of the aerodynamic lens accelerates the particles to a terminal velocity depending on their size (Drewnick et al. 2005). A mechanical chopper is located in the ToF region. The chopper can use two slits in particle time-of-flight mode (PToF) or multiple slits allowing approximately 50 % of the particles to pass in efficient PToF (ePToF) mode. The advantage of ePToF is its good resolution and high signal-to-noise ratio (Campuzano-Jost et al. 2014). Particle size information is gained when the chopper rotates and allows particles through periodically (Drewnick et al. 2005).

Particles with differing diameters reach differing terminal velocities after the nozzle expansion of the aerodynamic lens. Equation 4.8 shows this velocity, which can be used for calculating d_{va} for the particles. The equation is based on modelled data and calibration procedures are in place for calculating the constants in the equations. (Jayne et al. 2000; Allan et al. 2003)

Apart from the PToF mode, the chopper can be operated in mass spectrum (MS) mode. In MS mode, the chopper can be in a closed or open position. In the closed position, the chopper blocks the particle beam, while the open position allows everything to pass into the instrument (Jimenez et al. 2003). The resulting mass spectra is the difference between the closed background spectra and the open measured spectra. Typically the chopper is operated so that it switches between different modes automatically. The length of these modes can be adjusted to suit different purposes.

4.1.3 Vaporization and ionization

After the PToF region, the particles enter the vaporization and ionization chamber. In the standard AMS configuration, the particles are vaporized using a tungsten vaporizer. The vaporizer is porous and 20 % of the vaporizer volume is void. The front, is shaped

like an inverted cone. The porosity and the shape of the cone are chosen to capture bouncing particles. The temperature is measured using a micro thermocouple and the typical operating temperature is 600 °C with a power consumption of 2 W. (Drewnick et al. 2005)

The drawback of the tungsten vaporizer is that it can only vaporize non-refractory species (Drewnick et al. 2005), and that some semi-refractory species may have unwanted chemical reactions with the vaporizer. Semi-refractory species are also known to thermally decompose on the vaporizer surface, adding to the signal even with the chopper closed. (Drewnick et al. 2015) Onasch et al. (2012) have created a soot particle (SP) module for detecting black carbon and other refractory species including some metals. The laser vaporizer is based on the SP2 instrument (Schwarz et al. 2010), and it is a continuous wave laser with a diode pumped Nd:YAG intracavity with a wavelength of 1064 nm (Onasch et al. 2012).

The SP-module allows for quantification of non-refractory metals if they are collected on soot particles. The high vaporization temperature of black carbon induced by the laser (4000 °C, Moteki and Kondo 2010) is sufficient for flash vaporization of most metals. (Onasch et al. 2012; Carbone et al. 2015) Nilsson et al. (2015) have used the SP-AMS to measure metal particles, but lacked in the ability of defining correct relative ionization efficiencies (RIE) and were unable to quantify the signal.

Carbone et al. (2015) have added metals to aqueous solutions with regal black pigment. They have atomized these metallic solutions and calibrated RIEs for 13 different metals. They also compared the concentrations of metals acquired using these RIEs to other instruments in a field study and found better correlation with periods of high soot loadings. (Carbone et al. 2015) Saarikoski et al. (2017) have used the RIE values obtained by Carbone et al. (2015) for quantifying metals in the exhausts of city busses, relying again on having enough BC in the sample.

The SP-AMS can be operated in three different vaporization modes. The following two paragraphs are based on Avery et al. (2020). The first operation mode is tungsten vaporizer (TV), where only the tungsten vaporizer is used. This mode is identical to operation of a standard AMS. The second mode of operation is laser vaporizer (LV), where the tungsten vaporizer is removed and the laser vaporizer is on. In LV mode, the tungsten vaporizer has to be removed, due to it vaporizing some species, even when it has been set to the lowest possible setting. Removing the tungsten vaporizer is time consuming which makes swithcing between LV and TV modes impractical.

The final mode is dual vaporizer (DV), where both vaporizers are working. In DV mode, non-refractory and refractory species can be measured simultaneously. In DV mode, the laser can be swithced on and off rapidly, and the two results can be compared to get an understanding of the refractory particles without removing the tungsten vaporizer. The

DV modes with the laser on or off have different sensitivities for non-refractory species making interpretation of results difficult. The reason for this difference is complicated and one explanation is that the vaporizers have different collection efficiencies depending on particle size, shape and composition.

After vaporization, the particles are ionized. The tungsten vaporizer is mounted in the middle of the ionizer to have all vaporized molecules ionized. The ionizer is a commercially available 70 eV electron ionizer that emits the electrons from a tungsten filament next to the ion source, the ions are then extracted from the chamber by a lens with a potential of -100 V. (Drewnick et al. 2005) The laser vaporizer is also located so that the particle beam is vaporized inside the ionizer (Onasch et al. 2012).

4.1.4 Mass spectrum region

The vaporized and ionized particles are transported to a orthogonal ToF extractor via electrostatic lenses (Drewnick et al. 2005). The HR-ToF-AMS can operate in two different mass spectrum configurations, where the ion path length is varied. In V-mode, the ions travel a path of 1.3 m and in W-mode, the distance is 2.9 m (DeCarlo et al. 2006). The paths for V-mode and W-mode are illustrated in Figure 4.1. These paths are much longer, than in the original AMS, where the flight path was 0.45 m (Jayne et al. 2000). This additional path length allows for high resolution analysis and detection of individual compounds.

The ions are extracted from the ToF extractor into the ToF section by a pulsing high voltage. After each pulse, the extractor refills with new ions, the fill up time depends on the mass to charge ratio (m/z) of the ions. The ions are then collected to a multichannel plate detector (MCP) and the signal is converted using a data acquisition card. The raw mass spectra are averaged on the data acquisition card before being transferred to a PC. (Drewnick et al. 2005)

4.1.5 Calibration and data-analysis

The signal received by the MCP can be converted to mass concentration by doing a separate calibration measurement, where ionization efficiency is measured (Drewnick et al. 2005). The ionization efficiency calibration for the AMS is done using monodisperse NH_4NO_3 particles. A DMA (see section 3.2), which selects particles based on their electrical mobility or a centrifugal particle mass analyzer (CPMA, Olfert and Collings 2005), which selects particles based on their mass, can be used for creation of the monodisperse aerosol. The CPMA has a rotating cylinder and an electrical field. When the centrifugal and electrical forces are balanced, particles with a known mass-to-charge ratio can be transmitted. (Olfert and Collings 2005) The mass specific ionization efficiency can be

calculated

$$mIE_{\text{NO}_3} = \frac{10^{-12} \cdot IE_{\text{NO}_3} \cdot N_A}{M_{\text{NO}_3}}, \quad (4.14)$$

where 10^{-12} is used for unit conversions (mass unit of picograms), IE_{NO_3} is the nitrate ionization efficiency, $N_A = 6.022 \cdot 10^{22}$ is Avogadro's number and $M_{\text{NO}_3} = 62\text{g/mol}$ is the molar mass of NO_3 (Onasch et al. 2012). The mass concentration of a species (s) can be calculated

$$C_s = \frac{\sum_i I_{s,i}}{RIE_s \cdot mIE_{\text{NO}_3} \cdot Q}, \quad (4.15)$$

where $I_{s,i}$ is the ion rate, RIE_s is the relative ionization efficiency of a species (s) to nitrate, defined as equation 4.16 and Q is sample flow rate (Onasch et al. 2012).

$$RIE_s = \frac{mIE_s}{mIE_{\text{NO}_3}} \quad (4.16)$$

The calibration procedure for calculating the relative ionization efficiency for refractory black carbon RIE_{TBC} is similar to the procedure for calculating IE_{NO_3} . Size selected black carbon particles are analyzed using a condensation particle counter (CPC) and the AMS, and the calculated masses are used to determine RIE_{TBC} (Onasch et al. 2012). In the calibrations detailed by Onasch et al. (2012), the black carbon used was REGAL 400R pigment black, but recent discussion (Fortner and Avery 2023) has included a new pigment called Cab-O-Jet 300 (CB). The main advantage with CB particles is that it does not stain the measurement lines. The solution is also easier to maintain and doesn't require constant stirring. (Fortner and Avery 2023) Experimental work with CB has shown that it's properties accurately represent carbonaceous atmospheric aerosol and its spherical shape should allow for good lens transmission (Zangmeister et al. 2019).

Relative ionization efficiencies for different species can also be evaluated theoretically. Jimenez et al. (2003) propose that the relative ionization efficiency of a species (RIE_s) is directly proportional to the electron impact ionization cross section (σ) of the species, which can be found from literature. The number of electrons in an atom (N_e) is proportional to the molar mass of a species (Jimenez et al. 2003). Carbone et al. (2015) show that the relative ionization efficiency compared to another species can be calculated from

$$RIE_s = \frac{\sigma_{s1}}{N_{e,s1}} / \frac{\sigma_{s2}}{N_{e,s2}}. \quad (4.17)$$

Murphy (2016b) proposes that heavier molecules spend more time in the ionization region in the AMS, meaning that relative ionization efficiencies can not be calculated from

Table 4.1. Detection limits for non-refractory species measured by V-mode HR-AMS based on DeCarlo et al. (2006) and refractory black carbon measured by SP-AMS based on Onasch et al. (2012). Sampling time of 1 minute is used.

Species	DL (ng/m ³)
Organics	22
Sulfate	5.2
Nitrate	2.9
Ammonium	38
Chloride	12
Refractory black carbon	30

equation 4.17. Jimenez et al. (2016) and Murphy (2016a) continued this discussion and it is quite opinionated. Many processes govern the ionization and vaporization processes and the best way to estimate relative ionization efficiencies is by measurements (Nault et al. 2023). Equation 4.17 can be used for estimating RIE values but it can be unreliable for heavier molecules.

Detection limits of the AMS are defined as three times the standard deviation when measuring filtered air. The AMS is very sensitive and detection limits for different species measured in V-mode with 1-minute averages are presented in Table 4.1. The detection limits are in the range of 2.9 to 38 ng/m³. Sampling in W-mode can increase the detection limits by a factor of 5 to 15. (DeCarlo et al. 2006)

The data acquisition card saves the data in hdf5-format on the hard-drive of the PC. Wavemetrics' Igor Pro 9 is used for the analysis with extensions SQUIRREL and PIKA. SQUIRREL is used for unit mass resolution (UMR) analysis and PIKA is used for high resolution (HR) analysis.

During vaporization, the particles fragment into different molecules. The signal from these molecules is larger at lower m/z peaks, but reduced at higher m/z peaks. These fragmentation patterns are known and the timing of the molecules can be used to determine the composition of the original particle. Fragmentation tables are available for this reason. (Allan et al. 2004) They are important when analyzing the results and interpreting signals from certain species.

The IE and RIE_{rBC} values determined from the calibrations are input to the software to get accurate mass readings. The data-analysis process begins with the m/z -calibration, where known peaks are detected from the data and a fit is created to use the same calibration for all m/z -ratios. Next, a baseline is created to remove noise from the data using readymade functions in SQUIRREL. (Sueper 2024)

The signal generated by a single ion slowly reduces due to the performance of the elec-

tron amplification chain deteriorating. A correction factor is calculated using signals related to the air beam (m/z 28 or m/z 32). The flow rate is also accounted for due to the critical orifice collecting particles and becoming slightly blocked during measurement. The signal detected due to the air beam is proportional to the flow rate and a constant offset. A correction factor is calculated using these details and applied in the data analysis. (Allan et al. 2003) After these steps the data can be analyzed in unit mass resolution.

The high resolution analysis starts by finding the correct peak shape. The peak shape is of the form

$$P_i(t) = h e^{-((t-t_0)/\sigma)^2} f\left(\frac{t-t_0}{\sigma}\right), \quad (4.18)$$

where $P_i(t)$ is peak intensity for one ion as a function of ToF (t), h is a peak intensity parameter, t_0 is the ToF for the exact mass based on the m/z calibration, σ is the Gaussian peak width and f is a custom function that accounts for deviations from a Gaussian peak shape (DeCarlo et al. 2006). The peak shape is chosen by selecting known ions at several m/z values and combining them to form a peak fit. The fit is later used for separating signals of overlapping ions.

The calculated peak function is fit to all m/z in a certain area of interest. For example, starting from m/z 12 to 120, or even further if there is signal that can be interpreted. The user has to manually choose which ions to fit on all m/z . Some m/z only include a single ion, and some m/z contain multiple. The total signal for a chosen m/z is the sum of all signals of individual ions

$$P(t) = \sum_{i=0}^n P_i(t), \quad (4.19)$$

where $P_i(t)$ is the signal for a single ion and n is the number of ions (DeCarlo et al. 2006). Once all ions are fit, the dataset is ready, but has to be corrected.

The signal at m/z 29 usually consists of two ions, $^{15}\text{NN}^+$ and CHO^+ . To get a proper concentration of these two ions, the signal has to be corrected using the j15NN-correction. Next there is the CO_2 -correction, which is used to find the proportion of CO_2 in the gas phase and particle phase. The correction is done using data collected by a CO_2 sensor that is sampling next to the AMS. (Sueper 2024)

Now, the ratios between different atoms can be calculated, mainly H/C and O/C, for which the method is presented by Aiken et al. (2007). Canagaratna et al. (2015) have corrected the calculations of Aiken et al. (2007) and have introduced new calculations for elemental analysis, which can also be performed in PIKA. The AMS mass concentrations are typically calculated with a collection efficiency of 0.5 (Canagaratna et al. 2007), but Middlebrook et al. (2012) have introduced a method for calculating the composition dependent collection efficiency (CDCE) when sampling in TV-mode, which can also be calculated in PIKA.

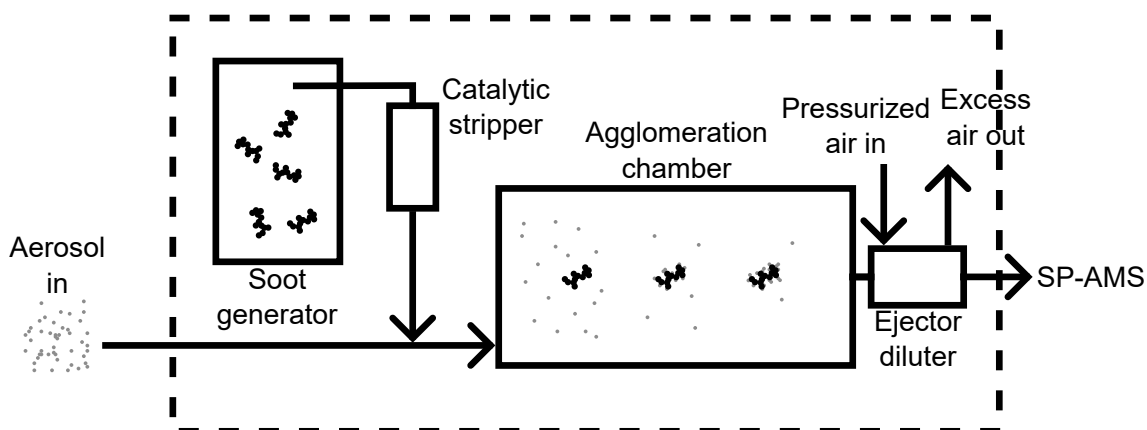


Figure 4.3. The concept of the soot particle agglomeration inlet (SPAI) adapted from Martikainen et al. (2021).

Now, the high resolution data can be used, and it is usually split into different categories, such as organics, sulfates or refractory black carbon to help with interpreting the results. These categories can include hundreds of different molecules. Sometimes the data can be analyzed even further, and for example, the oxidation of the organics can be analyzed. Another common analysis method with AMS data is positive matrix factorization (PMF), which can be used for source apportionment of the organic or inorganic fractions (Paatero and Tapper 1994; Ulbrich et al. 2009).

4.1.6 Soot particle agglomeration inlet (SPAI)

Due to the SP-AMS' limited ability to detect nanoparticles (P. S. K. Liu et al. 2007), Martikainen et al. (2021) have developed the soot particle agglomeration inlet (SPAI). As discussed in subsection 4.1.3, only particles vaporized by the tungsten vaporizer or the laser vaporizer can be detected. Martikainen et al. (2021) used soot particles for lens transmission and a chamber for agglomerating the test particles on the soot. The soot was chosen because of the high evaporation temperature induced by the laser that would also evaporate content attached to the soot particles that would otherwise be undetected (Martikainen et al. 2021).

The following description of SPAI is based on Martikainen et al. (2021). The sample flow is created using an ejector diluter (ED, Abdul-Khalek et al. 1998). The sampled particles are mixed with soot and led to an agglomeration chamber with a large volume resulting in a long residence time for agglomeration to take place. After the particles have agglomerated, the sample is led to the SP-AMS. The soot is produced using a flat flame acetylene burner, but it is noted that any device capable of generating soot particles can be used. A catalytic stripper (CS, Abdul-Khalek and Kittelson 1995) is used to remove volatile compounds with the goal of leaving only non-volatile soot particles. The concept of the SPAI can be seen in Figure 4.3.

Martikainen et al. (2021) proved the concept of SPAI by sampling silver nanoparticles generated in a tube furnace. The detection factor of silver was improved by a factor up to 35. They also noted that the instrument was not calibrated for silver, which explains that the mass is not accurate. Particles would also not reach the detection region of the SP-AMS due to agglomeration with particles of undesired sizes. (Martikainen et al. 2021)

4.2 Alternative methods for nanoparticle chemical composition analysis

As discussed in subsection 4.1.1, the AMS detection range is limited to approximately 50–1000 nm particles. Other methods have been developed for measuring the chemical composition of particles smaller than 50 nm, but they are limited in some ways.

There are two main categories for nanoparticle chemical composition analysis methods. Filter methods include collecting sample on a filter and later analyzing it in the laboratory. Continuous methods include sample collection and analysis in the same system and can often be run on a relatively fast cycle. (Kulkarni et al. 2011)

Filters are one of the main ways of collecting particles for analysis. Filters use diffusion to collect the smallest particles and interception or impaction to collect large particles (Hinds 1999). Organic species are often measured from filter samples. The sample collection often requires extended periods of time and artifacts affecting the result can occur and precautions need to be taken in sample preparation, handling and extraction. Nonpolar and polar compounds are treated differently. Trace elements can also be analyzed from filter samples. (Kulkarni et al. 2011) Thermal desorption-gas chromatography/mass spectrometry (TD-GC/MS) can be used for faster analysis of these filter samples (Chow et al. 2007).

If one is interested in nanoparticles, an impactor (Hinds 1999, p. 121) could be used to remove particles above a desired diameter. Nanoparticles have very little mass, which increases the collection time considerably. Also the time resolution of a sample is almost non-existent, as collection takes a long time. For these reasons, filter collection is not suitable for real time nanoparticle chemical composition analysis.

The elemental composition of individual particles can be measured using transmission electron microscopy (TEM). An X-ray energy-dispersive spectrometer (XEDS) is needed in addition to the TEM for elemental analysis. This approach also requires sample collection on a grid suitable for TEM usage, limiting the time resolution. The analysis is restricted to single particles and can be relatively slow and biased if some particles are collected more efficiently than others. (Williams and Carter 2009)

Continuous methods can be used for analyzing concentrations of elemental carbon (EC), organic carbon (OC) and black carbon (BC). OC and EC are often differentiated according

to the temperature they evolve at. The evolved sample is converted to CO_2 or CH_4 and then detected. (Watson et al. 2005) Many different methods for OC and EC analysis are reviewed by Watson et al. (2005). These systems have residence times of several minutes (Watson et al. 2005) and nanoparticle detection could be limited if an impactor was used due to the low mass collected. BC is often detected using optical methods with an aethalometer, which can have a very good time resolution (Hansen et al. 1984; Drinovec et al. 2015). Thermal desorption methods can also be used in continuous measurements (Chow et al. 2007).

Trace elements can be measured using inductively coupled plasma mass spectrometry (ICP-MS, Houk et al. 1980). Traditionally, ICP-MS instruments have sampled from a liquid solution created by filter sampling, which requires a lot of work (Kulkarni et al. 2011). The ICP-MS can also be operated by sampling dry aerosols. Hess et al. (2015) have used the ICP-MS to measure aerosol and they have included an SMPS to measure size resolved chemical composition of small particles. The instruments struggles with a high detection limit making the sampling of the smallest particles difficult (Hess et al. 2015).

Instruments based on X-ray fluorescence (XRF) can be used for measuring metals. Most XRF instruments used for aerosol purposes consist of a filter tape which is analyzed periodically. XRF instruments are continuous but still have measurement times of several minutes, depending on the concentration of the sample. (Yanca et al. 2006)

S. Wang et al. (2006) introduced the nanoaerosol mass spectrometer (NAMS) for elemental analysis of individual nanoparticles. The NAMS is in principle quite similar to the AMS, as it has an aerodynamic lens, a vaporizer and a time-of-flight region for mass analysis. The NAMS uses a modified aerodynamic lens allowing moderate transport of particles below 50 nm and leaving most of particles larger than 50 nm out of the instrument. The instrument has noticeable losses and the ability to not detect particles above 50 nm is restricting. The instrument can be used for analyzing single particles, but has quite limited uses. (S. Wang et al. 2006)

Chemical ionization mass spectrometry (CIMS) can be used for real time measurement of atmospheric trace gases. The use of chemical ionization does not fragment the measured species as with the AMS. (Bertram et al. 2011) CIMS has been developed to measure trace gases but different inlet systems have been invented for measurement of organic aerosol in the particle phase.

The filter inlet for gases and aerosols (FIGAERO) is an inlet capable of collecting particles on a filter while sampling gases. The filter is heated periodically and the collected aerosol is measured based on temperature dependent thermal desorption. (Lopez-Hilfiker et al. 2014)

Another inlet for the CIMS developed by Lopez-Hilfiker et al. (2019) is the extractive elec-

troscopy ionization (EESI). The EESI relies on extracting soluble components created by an electrospray. The EESI samples at a much faster time resolution and transmission of particles between 20 and 750 nm is greater than 80 %. (Lopez-Hilfiker et al. 2019) These inlets coupled with a CIMS are only capable of detecting organic aerosol and they also the capability of measuring mass concentrations.

The methods for nanoparticle chemical analysis presented in this section can be run either continuously or by collecting particles on filters. If a filter is used, the collection time is long and time resolution is often lost. Continuous methods can be used for detecting selected species. All of these methods suffer from a low detection limit if the particle mass is small. Single particles can also be analyzed, but many particles need to be analyzed to get a proper understanding of an aerosol. No instrument exists that can measure the chemical composition of nanoparticles in real-time calling for the development of an instrument for this application.

5. DEVELOPMENT AND CHARACTERIZATION

The design of the inlet system created in this thesis is based on SPAI. Martikainen et al. (2021) concluded that SPAI could be improved by finding the optimal size distribution for soot that would pass the aerodynamic lens. They also discussed some pre-treatment options for different samples. The main difference between SPAI and the system designed in this thesis is the generation method for the soot particles.

A problem with the SPAI is that the soot generation requires a burning flame. The soot particles also need to be treated by the CS and constant flow of N_2 is required. These components make the burner less viable for field studies and a more compact and versatile method would be useful. Composition of particles that are similar to the produced soot can not be studied with the AMS limiting the use of the SPAI to materials that are not carbonaceous.

5.1 Development

The inlet system in this thesis generates the particles using an atomizer. Cab-O-Jet 300 (CB) was chosen as the solution for particle generation. CB mimics the properties of black carbon and is highly absorbing (Zangmeister et al. 2019), meaning that the SP-module of the AMS should evaporate the material efficiently. CB has an effective density of around 0.8 g/cm^3 and particle size can range from dozens of nanometers to hundreds depending on the concentration of the solution (Zangmeister et al. 2019).

Salt particles can also be used as agglomeration particles. The same atomizer can be run using a solution of a salt. NaCl is optimal for this purpose as it is easy to acquire and particles can be generated using an atomizer. NaCl does not overlap with any major ions in the AMS spectra making measurement of non-refractory species that are not chlorides possible. If a sample included refractory metals, CB could be used and if the sample consisted of organics, NaCl could be used. The atomizer also allows for use of other solutions that a user can create to best suit their needs, expanding the usability of the instrument.

The atomizer used in this thesis is a commercially available Topas ATM 220 atomizer (Topas GmbH 2024), which was chosen as it requires only an input of pressurized air

making it field deployable. The atomized particles are dried using the Topas DDU 570/H diffusion dryer unit (Topas GmbH 2025), as it is also relatively cheap and easy to maintain. A double helical ribbon static mixer is used for homogenizing the sample flow with the atomizer flow (Ghanem et al. 2014).

The flow in the chamber is kept laminar with $Re < 2300$, where Re is the Reynolds number for tube flow

$$Re = \frac{VL\rho}{\mu}, \quad (5.1)$$

where V is the fluid velocity, L is a characteristic length, typically the diameter of a pipe and ρ and μ are the density and dynamic viscosity of the fluid respectively (Spurk and Aksel 2008). The flow is kept laminar to mitigate mixing, which is required to distinguish single events from the data. A half-cone angle of 5° or less does not cause flow separation (Sparrow et al. 2009), but can be hard to manufacture. The inlet should be built with as low of a half-cone angle as possible, but with the limitations of manufacturing and field-deployability in mind.

The flow through the agglomeration chamber is kept constant with a commercially available ejector diluter (ED). The ED is suitable for this purpose as there are no moving parts and only pressurized air is required to run it. The ED is followed by a static mixer to mix the sample after the ejector. After the ED, the pressure is equalized and the sample is taken to the SP-AMS.

The modifiable parameters that are chosen in this thesis are particle generation and residence time. First an experiment was made to find how the concentration of the solution and the inlet pressure of the atomizer affected the resulting particle size distribution. When suitable distributions were found, multiple residence times and sample concentrations were tested to see how much time the particles needed for sufficient agglomeration.

5.1.1 Particle generation

The operating parameters for the atomizer were chosen by sampling solutions of different concentrations with different atomizer inlet pressures. The sampling setup is presented in Figure 5.1 and it consisted of the atomizer, a self made silica diffusion dryer, a flow meter and an SMPS consisting of a TSI DMA 3081 and TSI CPC 3775. The CPC flow rate was 0.3 lpm and the sheath flow in the DMA was 3 lpm. The SMPS was run with a scan time of 120 s and a return time of 15 s leaving 45 s between each scan. All measurements included three scans and zero air was sampled to determine that the SMPS did not have a significant noise level. The CPC sampled mostly in count mode if the concentration was low enough. The CPC also sampled in the photometric mode for some tests but it should

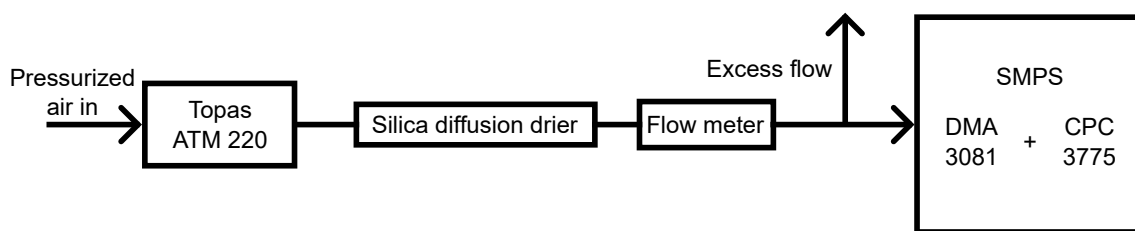


Figure 5.1. Measurement setup for atomizer tests. SMPS is the scanning mobility particle sizer consisting of a TSI DMA 3081 and a TSI CPC 3775.

not affect the result excessively. If similar experiments are carried out in the future, extra dilution should be applied to reduce the concentration below the photometric limit of the CPC.

The concentration of the CB solution was varied between 1 and 10 ml per 100 ml of purified water. The concentration of the NaCl solution was varied between 1 and 7 g per 100 ml of water. The atomizer pressure was varied between 1 and 3 bar for all solutions. KCl and Na₂SO₃ solutions with concentrations of 5 g per 100 ml of water were also measured to see how much of an effect changing the salt has on the resulting number size distribution.

After the measurements, the concentrations, geometric mean diameters (d_g) and fractions of particle number below 50 nm were calculated for CB and NaCl solutions. These results are presented in Figure 5.2. KCl and Na₂SO₃ solutions showed similar results to NaCl. They overlap more with common ions in the AMS spectra, so NaCl is chosen to be the superior solution for the atomizer.

The concentrations for both CB and NaCl increase as atomizer pressure is increased. CB concentrations also systematically increase as the solution is made stronger. NaCl does not show a similar result. The atomizer pressure does not have a significant effect on (d_g) of CB, but NaCl shows an increase when pressure is increased. The stronger the solution, larger the d_g for both solutions. The fraction of particles below 50 nm is decreased as the solutions are made stronger. Pressure does not seem to have a great effect on the fraction.

The NaCl solution produces higher particle numbers than CB, approximately 5 times more. The produced d_g s are similar but slightly higher for CB, which is a reason for why the fraction of particles below 50 nm is smaller for CB. The standard deviations presented as errorbars in Figure 5.2 show that the generated distribution is the least stable for low pressures and low concentrations.

These results show that the optimal distribution is realized when atomizer inlet pressure and concentration of the solution are increased. These can not be increased infinitely due to practical reasons. A high pressure of air can be hard to obtain during a field campaign. The NaCl solution showed signs of clogging the atomizer while sampling at high concen-

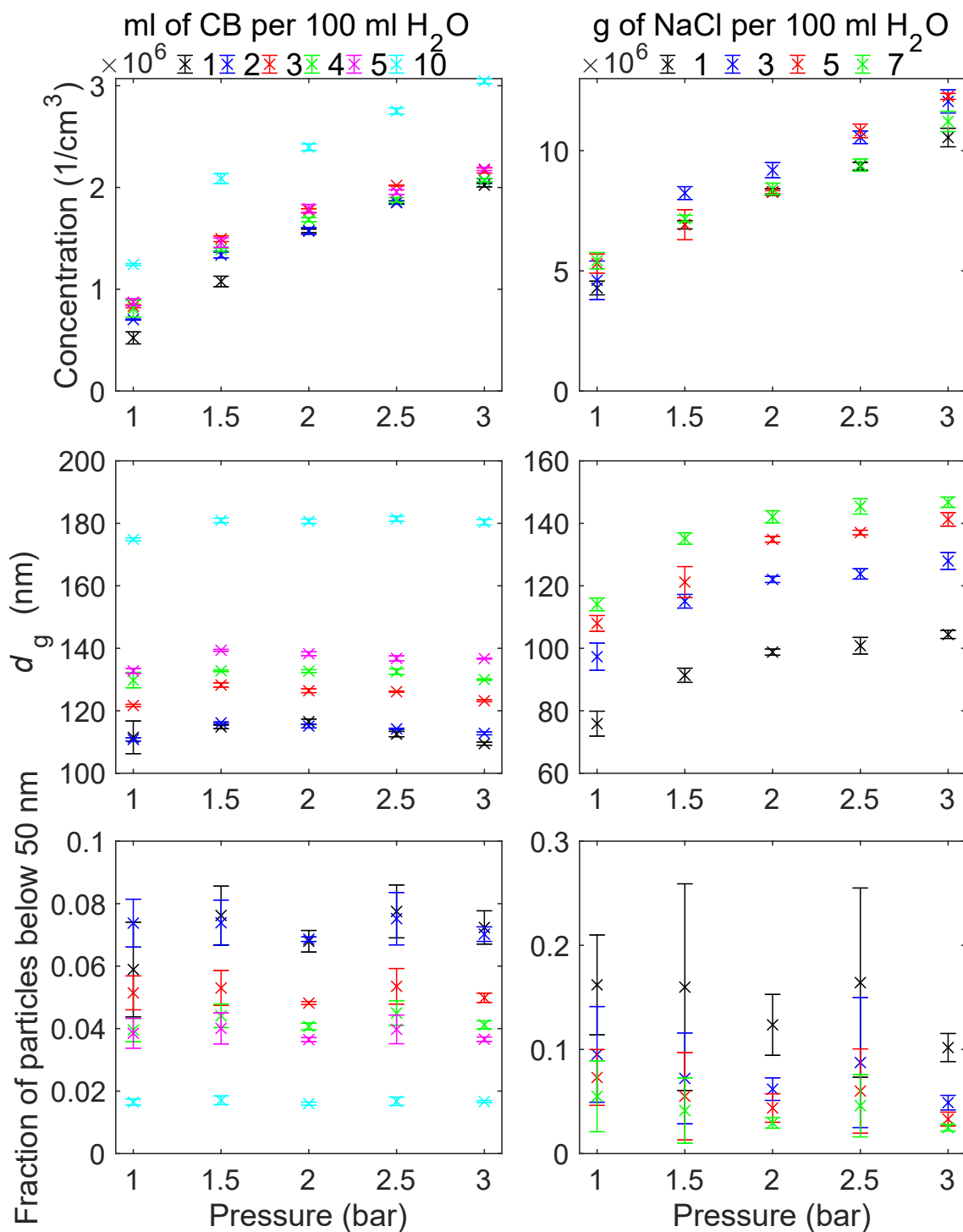


Figure 5.2. The number concentration (a,b), geometric mean diameter d_g (c,d) and fraction of particles below 50 nm (e,f) with standard deviations presented as errorbars for Cab-O-Jet 300 (a,c,e) and NaCl (b,d,f). The concentrations of the solutions are presented on top of each column.

trations making the use of a small concentration more favorable. A higher pressure also creates a higher flowrate which is needed if the sample has a high concentration and many agglomeration particles are required.

For CB, a solution of 10 ml per 100 ml of distilled water is chosen and for NaCl a solution of 5 g per 100 ml of water is chosen to try and minimize clogging while allowing for a good distribution. The atomizer pressure was chosen to be 3 bar for both solutions resulting in a flowrate of approximately 3.2 liters per minute. These settings can be varied later if some measurement scenario requires more or less particles of some type.

5.1.2 Residence time

The optimal residence times were acquired by sampling silver nanoparticles generated in a tube furnace and varying the concentration and residence time. The setup for these measurements can be seen in Figure 5.3. The setup contained the same atomizer and dryer used in the previous experiments. Extra dilution was achieved using pressurized air and a mass flow controller (MFC) after the diffusion dryer. Silver was generated using a heated tube furnace (1200 °C) with N₂ as the carrier gas. Pressurized air was used outside of the furnace for cooling of the silver aerosol. The two flows were mixed using a double helical ribbon static mixer. The combined aerosol was taken to a three way valve, where the aerosol entered the residence time tube (RTT) or a thin bypass line with minimal residence time. Constant flow was created using an ED coupled with a static mixer. The flow through the chamber was varied by adding extra dilution before the ED.

The sample was analyzed using two SMPS systems. One system included a TSI DMA 3085 and a CPC 3756 for sampling nanoparticles. The other included a TSI DMA 3081 and a CPC 3775 for sampling larger particles. The sample flow rates were 1.5 and 0.3 lpm with sheath flows of 15 and 3 lpm, respectively. The scan times and measurement procedures were identical to the distribution measurements described in section 5.1.1.

The flow through the test chamber was varied from approximately 2 to 6 lpm, which corresponds to residence times between 25 and 75 seconds. The volume of the residence time tube was 2.5 liters. The fraction of CB particles was varied between 1.5 and 65 % of the total particle number. The CB measurements consisted of six different concentrations and 5 residence times for each of them and a bypass measurement. Measurements with NaCl only included three concentrations as the main focus was kept on the CB measurements.

The data were analyzed by fitting a log-normal function to each SMPS scan for the silver and the CB distribution individually. Concentrations for the distributions were calculated based on these fits and. Dilution ratios were calculated based on the flows measured by the flowmeter and the flow input of the MFC after the RTT using equation

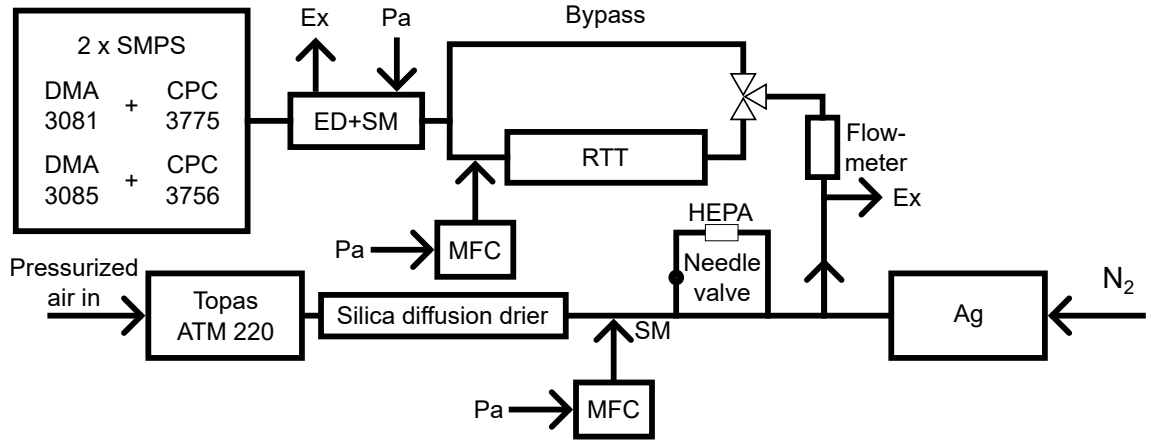


Figure 5.3. Measurement setup for residence time experiments. Two scanning mobility particle sizers (SMPS) were used consisting of a TSI DMA 3081 with a TSI CPC 3775 and a TSI DMA 3085 with a TSI CPC 3756. The silver aerosol generated in a tube furnace was carried by a nitrogen flow. Pressurized air (Pa) was input at multiple points and excess air (Ex) was removed to balance the pressure. Mass flow controllers (MFCs) were used to change the residence time and dilute the sample. Static mixers (SMs) were used at multiple points to mix different flows. A residence time tube (RTT) with a large volume was placed before an ejector diluter (ED).

$$DR = \frac{Q_{\text{sample}} + Q_{\text{dil}}}{Q_{\text{sample}}}, \quad (5.2)$$

where Q_{sample} is the flowrate measured by the flowmeter and Q_{dil} is the dilution flow input by the MFC. Residence times were calculated with equation

$$t = \frac{V}{Q_{\text{sample}}}, \quad (5.3)$$

where V is the volume of the RTT, 2.5 liters. The fraction of CB particles of the total particle number was calculated and plotted against residence time in Figure 5.4. The figure shows the fraction of CB particles during the bypass measurement in the legend and the fraction of CB particles after a certain residence time.

Figure 5.4 shows that if the fraction of CB particles is above 30 % of the total particle number, a large fraction of particles can be collected with a residence time well below 60 s. The three measurements with the highest starting concentrations of CB showed that more than 90 % of the particle number transferred to the CB distribution with a residence time of approximately 40 s or less.

These results show that the most important factor in the agglomeration of nanoparticles is sufficient number concentration of CB particles. When measuring with this inlet system, the user should be mindful of the number concentration of their sample and dilute the sample or adjust the residence time to have sufficient agglomeration. The recommenda-

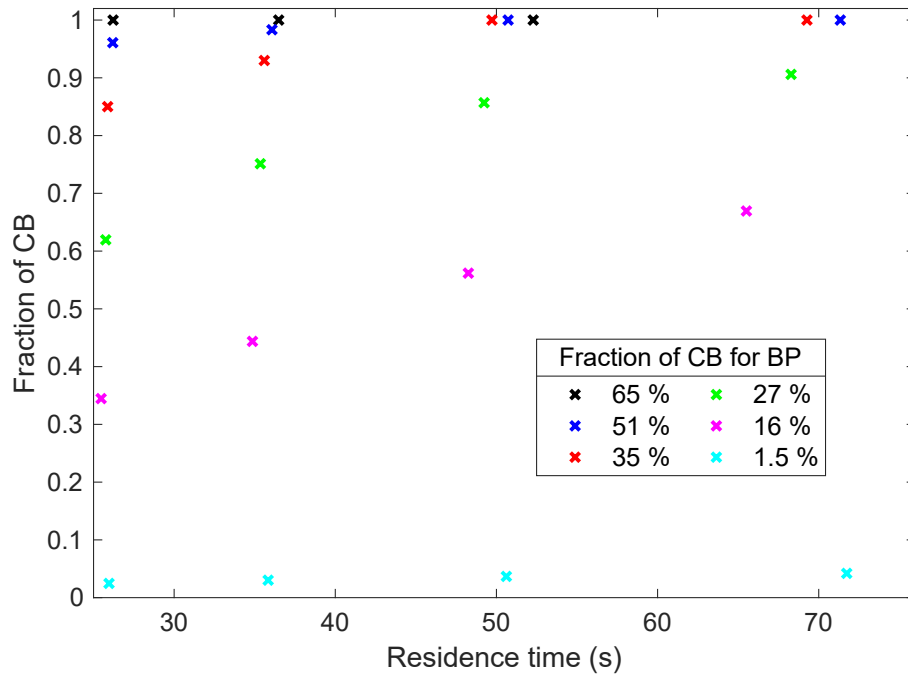


Figure 5.4. Results for the residence time experiments. Fraction of CB shows the fraction of total particle number for CB plotted against residence time. Legend shows the fraction of CB particles in the bypass (BP) measurements.

tion is that a residence time of 40 s should be used when the fraction of CB particles is approximately 30 % or higher for most of the measurement.

5.2 Design

The components of the inlet are presented in Figure 5.5. Pressurized air is lead to a Topas ATM 220 atomizer at a pressure of 3 bar, which is controlled by a pressure regulator. The solution for the atomizer is 10 ml CB per 100 ml of purified water. The aerosol from the atomizer is dried using a Topas DDU 570/H diffusion dryer. The RH after the dryer is measured using a cheap RH-sensor to detect when the dryer needs to be regenerated. The sample is connected to the flow at this point with a double helical ribbon static mixer for mixing of the flows.

The flowrate of the chamber is kept at 4.5 lpm, of which 3.2 lpm are from the atomizer and 1.3 lpm are from the sample. A residence time of 40 s can be obtained with a volume of 3 liters. The chamber is constructed of stainless steel to prevent corrosion and it is 67 cm long with an inner diameter of 72 mm and diffusers with a half cone angle of approximately 18° on both ends. The angle is larger than optimal due to the length of the cone and difficulties with manufacturing the parts. It will result in mild turbulence, but the flow is still quite laminar with a Reynolds number of $Re=90$. The residence time chamber is connected with 12 mm piping at both ends.

A self-made flowmeter with a critical orifice and pressure sensors is placed after the

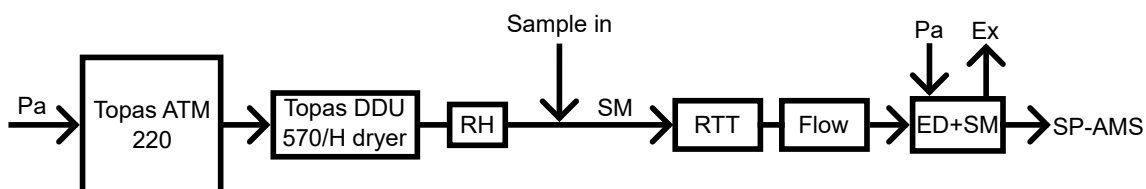


Figure 5.5. The components of the designed inlet system. Pressurized air (Pa) is used in the Topas ATM 220 atomizer and the resulting aerosol is dried with the Topas DDU 570/H dryer. A sensor for RH measurement is placed before the sample is taken in and mixed with the atomizer flow using a static mixer (SM). The flow is led to the residence time tube (RTT) and created by an ejector diluter (ED). It is measured by a flowmeter. The ED has an input of Pressurized air and also an exhaust line (Ex). The sample is taken to the SP-AMS after mixing of the ED exhaust using a static mixer.

chamber and before an ED. Pressurized air is led to the ED and controlled by a regulator. The exhaust line is kept open and should be properly handled when experimenting. The aerosol is then led to the SP-AMS. The maximum number concentration of the sample is $4 \cdot 10^6 \frac{1}{\text{cm}^3}$ based on the residence time and flow ratios.

These parts can be placed in a case similar to that of the SP-AMS. With the current design, different solutions can be run in the atomizer, but parts could also be exchanged and for instance, the atomizer could be bypassed to include another generation method with the same residence time chamber and flow designs.

5.3 Characterization

The transmission of nanoparticles, along with improved detection of metals will be assessed by sampling metal particles generated in a tube furnace. Experiments will be carried out for Ag, Al, Sn and Zn as they have low enough melting points, allowing particles to be generated in a furnace with a maximum temperature of 1200 °C.

The SP-AMS was calibrated with NH_4NO_3 and CB particles before and after the campaign. The setup is described by Onasch et al. (2012) with the addition of a CPMA after the DMA to have an exact measurement of mass per particle. A TSI DMA 3071 with a sheath flow of 6 lpm was used with the Cambustion CPMA Mk2 with diameter based resolution set to 10. A TSI CPC 3776 was measuring with a flowrate of 0.3 lpm.

The experimental setup is presented in Figure 5.6. Nitrogen gas is used as a carrier through the furnace, where different metals are kept in a ceramic boat. The furnace temperature is adjusted for each metal depending on their melting point. Melting points and used furnace temperatures are presented in Table 5.1.

The sample aerosol generated in the furnace is led through a DMA and a CPMA. The DMA is used to select a certain mobility, which is then located using a CPMA and a CPC to sample monodisperse particles with a known mass without disturbance from multiply

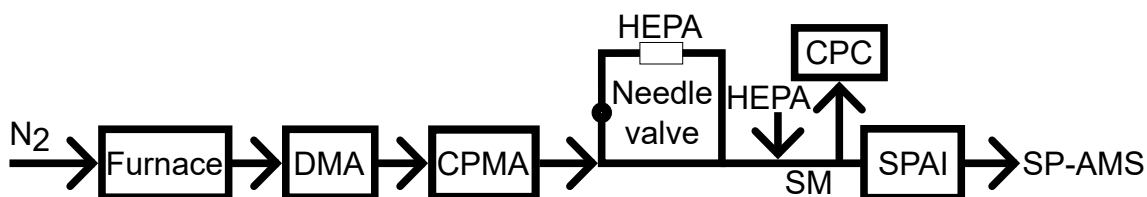


Figure 5.6. The setup used for calibration of relative ionization efficiencies and measurement of detection limits. A differential mobility analyzer (DMA) and a centrifugal particle mass analyzer (CPMA) are used for monodisperse aerosol creation. Filtered air is lead to the chamber to equalize the pressure before the sample is lead through a static mixer (SM) to a condensation particle counter (CPC) followed by the agglomeration inlet (SPAI) and the SP-AMS.

charged particles. A controllable diluter with a needle valve and a HEPA filter is used to vary the concentration of the aerosol. A static mixer is placed after the diluter to have a stable aerosol. The pressure is equalized with a HEPA filter before splitting the flow to a CPC and the agglomeration inlet placed before the SP-AMS.

The SP-AMS was run with a menu repeating 10 s chopper closed and 10 s open three times before averaging. An alternative menu with 15 s closed, 15 s open and 30 s PToF was also run to sample the size distribution of the sampled metals. The laser vaporizer was mostly turned on, but laser off experiments were also conducted for all metals. The chopper stopped functioning after the measurements with Ag and Zn and PToF data was not measured after that point.

The instrumentation consisted of a TSI DMA 3085 connected to TSI 3088 neutralizer. A Cambustion CPMA Mk2 is placed after the DMA and particles are counted with a TSI CPC 3776 with a flow rate of 0.3 lpm. The flow through the furnace was kept at 2 lpm by a mass flow controller. The DMA and CPMA sheath flow and resolution were varied for each case depending on the available particle size distribution. The resolution was kept as high as possible but some cases where particle mass was too low required lowering the resolution.

The particle size selected by these instruments also varied based on the available distribution. If the particle size was too small, the neutralizer suffered from a low charging efficiency and particles were lost in the DMA and if the size was increased too much, the use of the agglomeration chamber was not required. Selected mobility diameters ranged from 19 nm to 58 nm. The CPMA was used to locate the monodisperse peak with an input of bulk density in the software. All densities were below their bulk values but still quite close.

The dilution ratio of the ED was measured to be 2.8. The total dilution of the inlet was calculated based on the flowmeter. The total DR ranged from 8.5 to 10. The data was analyzed in Igor Pro 9 using extensions SQUIRREL v. 1.65 and PIKA v. 1.25. The steps

discussed in subsection 4.1.5 were followed in the analysis. The CPC data was directly logged on the AMS software.

The measurements included measurement of filtered air to check that there were no particles in the background air. CB particles were sampled on their own with filtered air coming into the agglomeration chamber to have a background signal of CB that can be later extracted from the measured signal. Mass spectra from these measurements is shown in Figure 5.7. The mass spectra has been corrected by relative ionization efficiencies of all measured species with a collection efficiency of 1. As can be seen, the mass spectra is dominated by carbon fragments ranging from C_1^+ to C_9^+ .

From Figure 5.7 one would assume that CB causes minimal interference as most of the signal is attributed to refractory BC. Some organic fragments can also be observed. The background signal from CB is in fact so large that even the almost invisible peaks cause signals of hundreds of Hz meaning that observation of material overlapping these signals is technically impossible as the detection limit is determined by three times the standard deviation of filtered air and CB sampled through the agglomeration chamber. Measurements of CB and filtered air with the laser vaporizer turned off showed a large background signal, indicating that the signal could be originating from the de-ionized water that is used as part of the CB solution.

The large mass defect of metals makes them candidates for having a clear signal that isn't affected by the CB signal. The experiments with the chosen metals proved that this is not the case. Al is located close to a large peak at m/z 27 meaning that quantification is impossible. With no stable isotopes, Al can not be evaluated based on them either. Sn also encountered a similar problem. Even though there are 10 stable isotopes of Sn, none of them showed enough signal to be quantifiable.

It could also be that there were problems with particle generation but it is highly unlikely as the tube furnace background was measured and was very low and the nitrogen flow would keep the particles from oxidizing. The use of a double classification system based on mobility and mass also showed that the densities of the particles are close to their bulk values indicating that the sampled materials are what they should be. Zero and background measurements also indicated that there were no particle sources affecting the experiments.

Other metals also showed a large background signal when sampling CB particles but no signal when sampling only filtered air. The most notable of these is Rb which was not input to the system at any time but showed a clear signal throughout the experiments when CB was sampled. Carbone et al. (2015) measured a much higher than theoretical relative ionization efficiency for Rb and suspected that the signal is coming from particles vaporizing on the hot surfaces of BC particles, which could also be the case in these experiments.

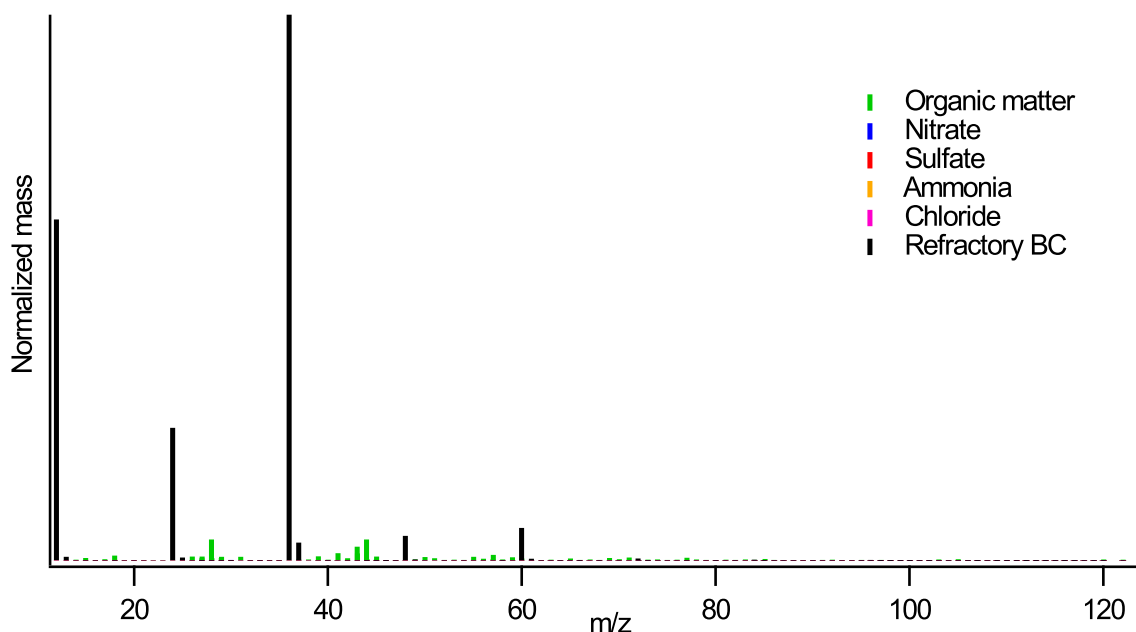


Figure 5.7. Normalized mass spectra of atomized Cab-O-Jet 300 particles. Relative ionization efficiencies of all species have been applied. A collection efficiency of 1 is assumed for all species.

Ag and Zn were quantifiable and also showed a background signal which could be originating from the same process. Zn with a low melting point of 419 °C could also be slowly vaporized by the tungsten vaporizer (Drewnick et al. 2015). Ag particles (19 nm) measured without the agglomeration inlet showed a signal below the detection limit, but Zn particles (58 nm) showed a signal even without the agglomeration inlet, as would be expected due to their size and melting point.

Figure 5.8 shows the calibration curves for (a) Ag and (b) Zn. The y-axis is SP-AMS Hz of all isotopes associated with the metal and x-axis is picograms per second put into the instrument and it is determined from the CPC counts, CPMA mass per particle and SP-AMS flowrate. The results showed more variance than usual for AMS data, most likely originating from the CB signal interference. The Ag calibration curve is well aligned with the origin of the graph, but there is an offset for Zn, most likely arising from imperfections with the background subtraction. The isotopic ratios measured correspond to known values, indicating that there are no major issues with the measurement.

The RIE-values calculated from the sensitivities presented in Figure 5.8 can be seen in Table 5.1 along with comparisons to theoretical values based on electron impact ionization cross sections calculated from equation 4.17. Detection limits presented as 3σ values of filtered air and CB measured with the averaging discussed above. Furnace temperatures and melting points are also presented.

The RIE value of Ag is quite low compared to its theoretical value. Carbone et al. (2015) reported similar values for Mn, Fe and Ni with no known reason causing this discrepancy.

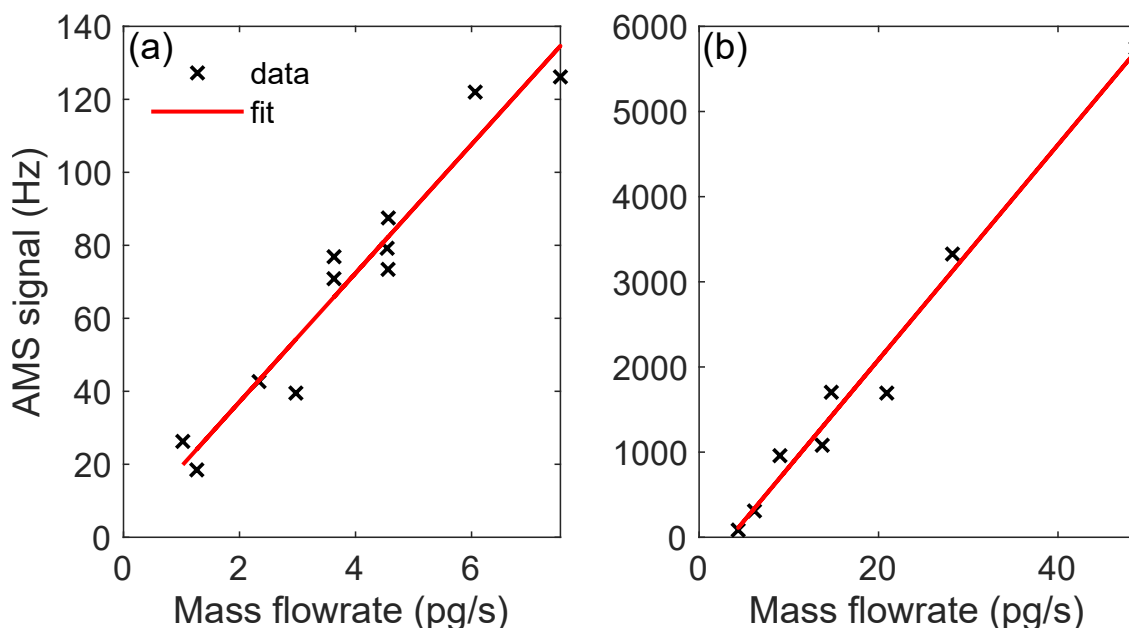


Figure 5.8. Calibration results for (a) silver (b) Zn. The y-axis is AMS signal (Hz) and x-axis is particle mass per second (pg/s) determined from the CPC signal.

Table 5.1. Electron impact ionization cross sections (σ , 70 eV), theoretical (t) and measured (m) relative ionization efficiencies to black carbon (RIE), detection limits (DL) of the measured materials as 3σ values of filtered air and CB with an averaging time of 1 minute, and melting points and used furnace temperatures for all materials.

Ion	σ (\AA^2)	RIE _t	RIE _m	RIE _m /RIE _t	DL (ng/m ³)	T_{melt} (°C)	T_{furn} (°C)
Ag ⁺	5.24 ^a	0.44	0.13	0.30	68	961 ^e	1200
Zn ⁺	3.66 ^b	0.48	0.94	1.96	77	419 ^f	700
C ₃ ⁺	4.43 ^c	1	1	1	30 ^d	-	-

^aFreund et al. (1990), ^bKaur et al. (2015), ^cNaghma and Antony (2013), ^dOnasch et al. (2012), Thermo Fisher Scientific Chemicals ^e(2009), ^f(2012).

Vaporizer effects discussed by Murphy (2016b) could play a role in this value. The RIE value of Zn is almost double of the theoretical value. This can be caused by slow vaporization processes in the tungsten vaporizer (Drewnick et al. 2015). Carbone et al. (2015) got a RIE value for Zn that was almost exactly the same as the theoretical value. They calculated the theoretical value with a different electron impact ionization cross section, which would change the ratio measured in this thesis to be 1.27.

The detection limits for Ag and Zn are 68 and 77 $\frac{\text{ng}}{\text{m}^3}$, respectively. They are quite high compared to ones listed in Table 4.1, but comparable to ones for metals reported by Carbone et al. (2015) indicating that the inlet has functioned well for its purpose. The dilution ratio has not been accounted for in the calculation and the true detection limits at the inlet side would be 590 and 730 $\frac{\text{ng}}{\text{m}^3}$, respectively. These detection limits are very hard to reach and limit the applicability of the instrument.

After the experiments, the cleanliness of parts of the agglomeration inlet was inspected. The RTT was visibly stained by CB particles, but cleaning was effortless with water and regular dish soap. Parts that could have been blocked were the ED, the flowmeter and the AMS critical orifice. The ED maintained a constant flow throughout the measurements and no residual was inspected when cleaning. The flowmeter critical orifice showed minor signs of obstruction, but was still operating effectively. The AMS flowrate remained constant and the critical orifice also showed no signs of clogging.

The AMS chopper had stopped working with ptof mode during the measurements. It was also inspected after the measurements and cleaned. It can not be said definitely that CB particles deposited on the chopper surface caused the IR trigger controlling the rotation to malfunction, but it is definitely a viable reason. Another reason could be that the chopper wiring was loose and was accidentally corrected at the same time. With inspection of the AMS, it was noticed that the exit of the aerodynamic lens had collected large amounts of CB.

5.4 Future developments

The measurements revealed that using CB as the agglomeration particles has the disadvantage of a very high background signal also on m/z values other than those of carbon fragments. The large mass defects of metals were not enough in all cases to distinguish their signal from neighboring ions. Only Ag and Zn from the sampled materials were quantifiable. The high detection limits caused by the dilution further discourage the use of CB for sampling metals in most scenarios.

This thesis focused on finding optimal parameters for running the agglomeration inlet. Section 5.1.1 shows how to find optimal size distributions for other agglomeration aerosols that could be used. Section 5.1.2 shows a detailed guide on how the residence time affects coagulation. Based on these experiments, other agglomeration aerosols could easily be optimized and used for lens transmission. This study also presents the parts required to build an agglomeration inlet using an atomizer.

Future work should focus on finding agglomeration aerosols that are purer and cause less interference on a range of m/z -values. Some options for these seed particles include using an atomizer with other diluters than water or using some type of heat treatment to purify the atomized aerosol. Other generation methods than atomizers should also be considered. Catalyzed burner soot should be revisited along with spark discharged carbon particles.

The main takeaway of this instrument is that each measurement scenario is different and researchers should generate their agglomeration aerosols for each purpose separately. A large library for the generation of agglomeration aerosols would require extensive lab-

oratory work and would benefit the end user with choosing the correct particles for their applications.

The inlet system could also be used with other instruments sharing a similar aerodynamic lens. Many cases where particle beams are required, would benefit from this system. For example, in X-ray photoelectron spectroscopy measurements where an identical aerodynamic lens to the one in the AMS has been used (Preger et al. 2024).

6. CONCLUSIONS

The aim of this thesis was to develop an inlet system for the soot particle aerosol mass spectrometer (SP-AMS) based on the principle presented by Martikainen et al. (2021) where soot particles are used as agglomeration particles for measured nanoparticles. The aim was to build a field-deployable inlet system that could be applied to a variety of measurement scenarios.

To support the field-deployability and use with different agglomeration particles, an atomizer was chosen for the generation of agglomeration particles. As soot particles have a higher vaporization temperature caused by the laser vaporizer, they are optimal for research of metals and other refractory species, which is why Cab-O-Jet 300 (CB) was chosen as the primary agglomeration particles for this thesis. Other agglomeration particles were successfully generated in subsection 5.1.1.

With a known distribution of agglomeration particles, the residence times required for collection of nanoparticles on the agglomeration particles surfaces were studied in subsection 5.1.2. The experiments conducted in both of these sections can be applied in the future with new agglomeration particles required for different measurements. With the residence time results, a residence time chamber was constructed to allow a large concentration of nanoparticles to be sampled without losing the time-resolution caused by a large residence time.

With known atomizer settings, residence time and flow settings, the agglomeration inlet was designed in section 5.2. Experiments described in section 5.3 were conducted to observe how functional the inlet is. The experiments included sampling of nanoparticles generated by four different metals. Calibration curves and detection limits were determined for Ag and Zn, but Al and Sn were non-quantifiable.

Ag detection without the inlet was not possible, proving the function of the system. Zn was detected also without the inlet due to properties discussed in section 5.3, but the sensitivity of the SP-AMS was still increased by the inlet. The inability to detect Al and Sn was attributed to the high background signal originating from CB particles. The residual from the atomizer caused an extensive background signal and the large mass defect of metals was not enough to distinguish Al and Sn from the CB background.

Although the instrument is not perfect and real world scenarios where it would be useful

with the agglomeration particles presented in this thesis are scarce, the experiments produced in this thesis are a building block for future development. The information about size distributions and residence times is invaluable when producing particles for future use. The aim of this thesis was reached by creating a strong background for how the inlet system should be operated and how future users can improve it to suit their needs.

Future developments discussed in section 5.4 are only a fraction of potential ideas that could be used for optimizing the instrument. Future work is crucial for accurate measurement of the chemical composition of nanoparticles and further development and experimentation should be continued.

REFERENCES

- Abdul-Khalek, I. S. and D. B. Kittelson (1995). "Real time measurement of volatile and solid exhaust particles using a catalytic stripper". In: *SAE transactions*, pp. 462–478.
- Abdul-Khalek, I. S., D. B. Kittelson, B. R. Graskow, Q. Wei, and F. Brear (1998). "Diesel exhaust particle size: measurement issues and trends". In: *SAE transactions*, pp. 683–696.
- Agarwal, J. K. and G. J. Sem (1980). "Continuous flow, single-particle-counting condensation nucleus counter". In: *Journal of Aerosol Science* 11.4, pp. 343–357.
- Aiken, A. C., P. F. DeCarlo, and J. L. Jimenez (2007). "Elemental analysis of organic species with electron ionization high-resolution mass spectrometry". In: *Analytical chemistry* 79.21, pp. 8350–8358.
- Aitken, J. (1888). "I. – On the number of dust particles in the atmosphere". In: *Earth and Environmental Science Transactions of The Royal Society of Edinburgh* 35.1, pp. 1–19.
- Allan, J. D., A. E. Delia, H. Coe, K. N. Bower, M. R. Alfarra, J. L. Jimenez, A. M. Middlebrook, F. Drewnick, T. B. Onasch, and M. R. Canagaratna (2004). "A generalised method for the extraction of chemically resolved mass spectra from Aerodyne aerosol mass spectrometer data". In: *Journal of Aerosol Science* 35.7, pp. 909–922.
- Allan, J. D., J. L. Jimenez, P. I. Williams, M. R. Alfarra, K. N. Bower, J. T. Jayne, H. Coe, and D. R. Worsnop (2003). "Quantitative sampling using an Aerodyne aerosol mass spectrometer 1. Techniques of data interpretation and error analysis". In: *Journal of Geophysical Research: Atmospheres* 108.D3.
- Avery, A. M., L. R. Williams, E. C. Fortner, W. A. Robinson, and T. B. Onasch (2020). "Particle detection using the dual-vaporizer configuration of the soot particle Aerosol Mass Spectrometer (SP-AMS)". In: *Aerosol Science and Technology* 55.3, pp. 254–267.
- Backman, U., J. K. Jokiniemi, A. Auvinen, and K. E. Lehtinen (2002). "The effect of boundary conditions on gas-phase synthesised silver nanoparticles". In: *Journal of nanoparticle Research* 4, pp. 325–335.
- Bertram, T. H., J. R. Kimmel, T. A. Crisp, O. S. Ryder, R. L. N. Yatavelli, J. A. Thornton, M. J. Cubison, M. Gonin, and D. R. Worsnop (2011). "A field-deployable, chemical ionization time-of-flight mass spectrometer". In: *Atmospheric Measurement Techniques* 4.7, pp. 1471–1479.
- Booth, B. and N. Bellouin (2015). "Climate change: Black carbon and atmospheric feedbacks". In: *Nature (London)* 519.7542, pp. 167–168.

- Campuzano-Jost, P., J. Jimenez, J. Kimmel, D. Day, W. Hu, D. Sueper, R. Knochenmuss, D. Worsnop, and J. Jayne (2014). "Particle Time-of-Flight by Hadamard Transform (ePTOF): A new high-duty-cycle approach to size-segregated and total aerosol mass measurements for the Aerodyne Aerosol Mass Spectrometer". In: *AGU Fall Meeting Abstracts*. Vol. 2014.
- Canagaratna, M. R., J. T. Jayne, J. L. Jimenez, J. D. Allan, M. R. Alfarra, Q. Zhang, T. B. Onasch, F. Drewnick, H. Coe, and A. Middlebrook (2007). "Chemical and microphysical characterization of ambient aerosols with the aerodyne aerosol mass spectrometer". In: *Mass spectrometry reviews* 26.2, pp. 185–222.
- Canagaratna, M. R., J. L. Jimenez, J. H. Kroll, Q. Chen, S. H. Kessler, P. Massoli, L. Hildebrandt Ruiz, E. C. Fortner, L. R. Williams, and K. R. Wilson (2015). "Elemental ratio measurements of organic compounds using aerosol mass spectrometry: characterization, improved calibration, and implications". In: *Atmospheric Chemistry and Physics* 15.1, pp. 253–272.
- Carbone, S., T. B. Onasch, S. Saarikoski, H. Timonen, K. Saarnio, D. Sueper, T. Rönkkö, L. Pirjola, A. Häyrinen, and D. Worsnop (2015). "Characterization of trace metals on soot aerosol particles with the SP-AMS: detection and quantification". In: *Atmospheric Measurement Techniques* 8.11, pp. 4803–4815.
- Chow, J. C., J. Z. Yu, J. G. Watson, S. S. Hang Ho, T. L. Bohannon, M. D. Hays, and K. K. Fung (2007). "The application of thermal methods for determining chemical composition of carbonaceous aerosols: A review". In: *Journal of Environmental Science and Health, Part A* 42.11, pp. 1521–1541.
- Chowdhury, S., A. Pozzer, A. Haines, K. Klingmueller, T. Münzel, P. Paasonen, A. Sharma, C. Venkataraman, and J. Lelieveld (2022). "Global health burden of ambient PM_{2.5} and the contribution of anthropogenic black carbon and organic aerosols". In: *Environment International* 159, p. 107020.
- Cohen, A. J., M. Brauer, R. Burnett, H. R. Anderson, J. Frostad, K. Estep, K. Balakrishnan, B. Brunekreef, L. Dandona, and R. Dandona (2017). "Estimates and 25-year trends of the global burden of disease attributable to ambient air pollution: an analysis of data from the Global Burden of Diseases Study 2015". In: *The lancet* 389.10082, pp. 1907–1918.
- Colbeck, I. and M. Lazaridis (2014). *Aerosol Science: Technology and Applications*. 1st ed. Newark: Wiley.
- DeCarlo, P. F., J. R. Kimmel, A. Trimborn, M. J. Northway, J. T. Jayne, A. C. Aiken, M. Gonin, K. Fuhrer, T. Horvath, and K. S. Docherty (2006). "Field-deployable, high-resolution, time-of-flight aerosol mass spectrometer". In: *Analytical chemistry* 78.24, pp. 8281–8289.
- DeCarlo, P. F., J. G. Slowik, D. R. Worsnop, P. Davidovits, and J. L. Jimenez (2004). "Particle morphology and density characterization by combined mobility and aerodynamic

- diameter measurements. Part 1: Theory". In: *Aerosol Science and Technology* 38.12, pp. 1185–1205.
- Drewnick, F., J.-M. Diesch, P. Faber, and S. Borrmann (2015). "Aerosol mass spectrometry: particle–vaporizer interactions and their consequences for the measurements". In: *Atmospheric Measurement Techniques* 8.9, pp. 3811–3830.
- Drewnick, F., S. S. Hings, P. F. DeCarlo, J. T. Jayne, M. Gonin, K. Fuhrer, S. Weimer, J. L. Jimenez, K. L. Demerjian, and S. Borrmann (2005). "A new time-of-flight aerosol mass spectrometer (TOF-AMS)—Instrument description and first field deployment". In: *Aerosol Science and Technology* 39.7, pp. 637–658.
- Drinovec, L., G. Močnik, P. Zotter, A. Prévôt, C. Ruckstuhl, E. Coz, M. Rupakheti, J. Sciare, T. Müller, and A. Wiedensohler (2015). "The" dual-spot" Aethalometer: an improved measurement of aerosol black carbon with real-time loading compensation". In: *Atmospheric measurement techniques* 8.5, pp. 1965–1979.
- Forster, P. T., K. Storelvmo, W. Armour, J.-L. Collins, D. Dufresne, D. Frame, T. Lunt, M. Mauritsen, M. Palmer, M. Watanabe, Wild, and H. Zhang (2021). "The Earth's energy budget, climate feedbacks, and climate sensitivity". In: *Climate Change 2021: The Physical Science Basis. Contribution of Working Group I to the Sixth Assessment Report of the Intergovernmental Panel on Climate Change*.
- Fortner, E. C. and A. M. Avery (2023). "SP-AMS/(LV-AMS) Updates and FAQ's". In: *2023 AMS/ACSM Users' Meeting*.
- Freund, R. S., R. C. Wetzel, R. J. Shul, and T. R. Hayes (1990). "Cross-section measurements for electron-impact ionization of atoms". In: *Physical Review A* 41.7, p. 3575.
- Friedlander, S. K. (2000). *Smoke, dust, and haze: fundamentals of aerosol dynamics*. New York: Oxford University Press.
- Fuchs, N. A. (1963). "On the stationary charge distribution on aerosol particles in a bipolar ionic atmosphere". In: *Geofisica pura e applicata* 56, pp. 185–193.
- Fuchs, N. A. and A. G. Sutugin (1971). "High-dispersed aerosols". In: *Topics in current aerosol research*. Elsevier, p. 1.
- Ghanem, A., T. Lemenand, D. Della Valle, and H. Peerhossaini (2014). "Static mixers: Mechanisms, applications, and characterization methods—A review". In: *Chemical engineering research and design* 92.2, pp. 205–228.
- Hansen, A. D., H. Rosen, and T. Novakov (1984). "The aethalometer—an instrument for the real-time measurement of optical absorption by aerosol particles". In: *Science of the Total Environment* 36, pp. 191–196.
- Hautanen, J., M. Kilpeläinen, E. I. Kauppinen, K. Lehtinen, and J. Jokiniemi (1995). "Electrical agglomeration of aerosol particles in an alternating electric field". In: *Aerosol Science and Technology* 22.2, pp. 181–189.
- Hess, A., M. Tarik, and C. Ludwig (2015). "A hyphenated smps–icpms coupling setup: Size-resolved element specific analysis of airborne nanoparticles". In: *Journal of Aerosol Science* 88, pp. 109–118.

- Hinds, W. C. (1999). *Aerosol technology : properties, behavior, and measurement of airborne particles*. 2nd ed. A Wiley-interscience publication. New York: Wiley.
- Hinze, J. O. (1955). "Fundamentals of the hydrodynamic mechanism of splitting in dispersion processes". In: *AIChE journal* 1.3, pp. 289–295.
- Hoppel, W. A. and G. M. Frick (1986). "Ion–aerosol attachment coefficients and the steady-state charge distribution on aerosols in a bipolar ion environment". In: *Aerosol Science and Technology* 5.1, pp. 1–21.
- Houk, R. S., V. A. Fassel, G. D. Flesch, H. J. Svec, A. L. Gray, and C. E. Taylor (1980). "Inductively coupled argon plasma as an ion source for mass spectrometric determination of trace elements". In: *Analytical Chemistry* 52.14, pp. 2283–2289.
- Jayne, J. T., D. C. Leard, X. Zhang, P. Davidovits, K. A. Smith, C. E. Kolb, and D. R. Worsnop (2000). "Development of an aerosol mass spectrometer for size and composition analysis of submicron particles". In: *Aerosol Science & Technology* 33.1-2, pp. 49–70.
- Jimenez, J. L., M. R. Canagaratna, F. Drewnick, J. D. Allan, M. R. Alfarra, A. M. Middlebrook, J. G. Slowik, Q. Zhang, H. Coe, and J. T. Jayne (2016). "Comment on "The effects of molecular weight and thermal decomposition on the sensitivity of a thermal desorption aerosol mass spectrometer"". In: *Aerosol Science and Technology* 50.9, pp. i–xv.
- Jimenez, J. L., J. T. Jayne, Q. Shi, C. E. Kolb, D. R. Worsnop, I. Yourshaw, J. H. Seinfeld, R. C. Flagan, X. Zhang, and K. A. Smith (2003). "Ambient aerosol sampling using the aerodyne aerosol mass spectrometer". In: *Journal of Geophysical Research: Atmospheres* 108.D7.
- Kaur, J., D. Gupta, R. Naghma, D. Ghoshal, and B. Antony (2015). "Electron impact ionization cross sections of atoms". In: *Canadian Journal of Physics* 93.6, pp. 617–625.
- Knutson, E. and K. Whitby (1975). "Aerosol classification by electric mobility: apparatus, theory, and applications". In: *Journal of Aerosol Science* 6.6, pp. 443–451.
- Kruis, F. E., H. Fissan, and B. Rellinghaus (2000). "Sintering and evaporation characteristics of gas-phase synthesis of size-selected PbS nanoparticles". In: *Materials Science and Engineering: B* 69, pp. 329–334.
- Kulkarni, P., P. A. Baron, and K. Willeke (2011). *Aerosol measurement : principles, techniques, and applications*. 3rd ed. Hoboken, N.J: Wiley.
- Kulmala, M., H. Vehkamäki, T. Petäjä, M. Dal Maso, A. Lauri, V.-M. Kerminen, W. Birmili, and P. McMurry (2004). "Formation and growth rates of ultrafine atmospheric particles: a review of observations". In: *Journal of aerosol science* 35.2, pp. 143–176.
- Lefebvre, A. H. (H. and V. G. McDonell (2017). *Atomization and sprays*. Second edition. Combustion: An International Series. Boca Raton: Taylor & Francis, CRC Press.
- Lelieveld, J., J. S. Evans, M. Fnais, D. Giannadaki, and A. Pozzer (2015). "The contribution of outdoor air pollution sources to premature mortality on a global scale". In: *Nature* 525.7569, pp. 367–371.

- Liu, B. Y. and K. Lee (1975). "An aerosol generator of high stability". In: *American Industrial Hygiene Association Journal* 36.12, pp. 861–865.
- Liu, P., P. J. Ziemann, D. B. Kittelson, and P. H. McMurry (1995a). "Generating particle beams of controlled dimensions and divergence: I. Theory of particle motion in aerodynamic lenses and nozzle expansions". In: *Aerosol Science and Technology* 22.3, pp. 293–313.
- Liu, P., P. J. Ziemann, D. B. Kittelson, and P. H. McMurry (1995b). "Generating particle beams of controlled dimensions and divergence: II. Experimental evaluation of particle motion in aerodynamic lenses and nozzle expansions". In: *Aerosol Science and Technology* 22.3, pp. 314–324.
- Liu, P. S. K., R. Deng, K. A. Smith, L. R. Williams, J. T. Jayne, M. R. Canagaratna, K. Moore, T. B. Onasch, D. R. Worsnop, and T. Deshler (2007). "Transmission efficiency of an aerodynamic focusing lens system: Comparison of model calculations and laboratory measurements for the Aerodyne Aerosol Mass Spectrometer". In: *Aerosol Science and Technology* 41.8, pp. 721–733.
- Lopez-Hilfiker, F. D., C. Mohr, M. Ehn, F. Rubach, E. Kleist, J. Wildt, T. F. Mentel, A. Lutz, M. Hallquist, and D. Worsnop (2014). "A novel method for online analysis of gas and particle composition: description and evaluation of a Filter Inlet for Gases and AEROSols (FIGAERO)". In: *Atmospheric Measurement Techniques* 7.4, pp. 983–1001.
- Lopez-Hilfiker, F. D., V. Pospisilova, W. Huang, M. Kalberer, C. Mohr, G. Stefenelli, J. A. Thornton, U. Baltensperger, A. S. Prevot, and J. G. Slowik (2019). "An extractive electrospray ionization time-of-flight mass spectrometer (EESI-TOF) for online measurement of atmospheric aerosol particles". In: *Atmospheric Measurement Techniques* 12.9, pp. 4867–4886.
- Magnusson, M. H., K. Deppert, J.-O. Malm, J.-O. Bovin, and L. Samuelson (1999). "Size-selected gold nanoparticles by aerosol technology". In: *Nanostructured Materials* 12.1-4, pp. 45–48.
- Martikainen, S., S. Saarikoski, P. Juuti, H. Timonen, J. Keskinen, and P. Karjalainen (2021). "Soot particle agglomeration inlet (Spai) for enabling online chemical composition measurement of nanoparticles with the aerosol mass spectrometer". In: *Aerosol and Air Quality Research* 21.6, p. 200638.
- Matthaios, V. N., J. Lawrence, M. A. Martins, S. T. Ferguson, J. M. Wolfson, R. M. Harrison, and P. Koutrakis (2022). "Quantifying factors affecting contributions of roadway exhaust and non-exhaust emissions to ambient PM_{10-2.5} and PM_{2.5-0.2} particles". In: *Science of The Total Environment* 835, p. 155368.
- May, K. (1973). "The Collison nebulizer: description, performance and application". In: *Journal of Aerosol Science* 4.3, pp. 235–243.
- Middlebrook, A. M., R. Bahreini, J. L. Jimenez, and M. R. Canagaratna (2012). "Evaluation of composition-dependent collection efficiencies for the aerodyne aerosol mass spectrometer using field data". In: *Aerosol Science and Technology* 46.3, pp. 258–271.

- Moteki, N. and Y. Kondo (2010). "Dependence of laser-induced incandescence on physical properties of black carbon aerosols: Measurements and theoretical interpretation". In: *Aerosol Science and Technology* 44.8, pp. 663–675.
- Murphy, D. M. (2016a). "Reply to "Comment on the effects of molecular weight and thermal decomposition on the sensitivity of a thermal desorption aerosol mass spectrometer" by Jimenez et al." In: *Aerosol Science and Technology* 50.12, pp. 1277–1283.
- Murphy, D. M. (2016b). "The effects of molecular weight and thermal decomposition on the sensitivity of a thermal desorption aerosol mass spectrometer". In: *Aerosol Science and Technology* 50.2, pp. 118–125.
- Naghma, R. and B. Antony (2013). "Electron impact ionization cross-section of C₂, C₃, Si₂, Si₃, SiC, SiC₂ and SiC₃". In: *Molecular Physics* 111.2, pp. 269–275.
- Nault, B. A., P. Croteau, J. Jayne, A. Williams, L. Williams, D. Worsnop, E. F. Katz, P. F. DeCarlo, and M. Canagaratna (2023). "Laboratory evaluation of organic aerosol relative ionization efficiencies in the aerodyne aerosol mass spectrometer and aerosol chemical speciation monitor". In: *Aerosol Science and Technology* 57.10, pp. 981–997.
- Nilsson, P. T., A. C. Eriksson, L. Ludvigsson, M. E. Messing, E. Z. Nordin, A. Gudmundsson, B. O. Mueller, K. Deppert, E. C. Fortner, and T. B. Onasch (2015). "In-situ characterization of metal nanoparticles and their organic coatings using laser-vaporization aerosol mass spectrometry". In: *Nano Research* 8, pp. 3780–3795.
- Olfert, J. and N. Collings (2005). "New method for particle mass classification—the Couette centrifugal particle mass analyzer". In: *Journal of Aerosol Science* 36.11, pp. 1338–1352.
- Onasch, T. B., A. Trimborn, E. C. Fortner, J. T. Jayne, G. L. Kok, L. R. Williams, P. Davidovits, and D. R. Worsnop (2012). "Soot particle aerosol mass spectrometer: development, validation, and initial application". In: *Aerosol Science and Technology* 46.7, pp. 804–817.
- Paatero, P. and U. Tapper (1994). "Positive matrix factorization: A non-negative factor model with optimal utilization of error estimates of data values". In: *Environmetrics* 5.2, pp. 111–126.
- Peck, J., L. A. Gonzalez, L. R. Williams, W. Xu, P. L. Croteau, M. T. Timko, J. T. Jayne, D. R. Worsnop, R. C. Mlake-Lye, and K. A. Smith (2016). "Development of an aerosol mass spectrometer lens system for PM_{2.5}". In: *Aerosol Science and Technology* 50.8, pp. 781–789.
- Preger, C., J. Rissler, A. Kivimäki, A. C. Eriksson, and N. Walsh (2024). "A versatile sample-delivery system for X-ray photoelectron spectroscopy of in-flight aerosols and free nanoparticles at MAX IV Laboratory". In: *Synchrotron Radiation* 31.5.
- Saarikoski, S., H. Timonen, S. Carbone, H. Kuuluvainen, J. Niemi, A. Kousa, T. Rönkkö, D. Worsnop, R. Hillamo, and L. Pirjola (2017). "Investigating the chemical species in submicron particles emitted by city buses". In: *Aerosol Science and Technology* 51.3, pp. 317–329.

- Sbai, S. E., C. Li, A. Boreave, N. Charbonnel, S. Perrier, P. Vernoux, F. Bentayeb, C. George, and S. Gil (2021). "Atmospheric photochemistry and secondary aerosol formation of urban air in Lyon, France". In: *Journal of Environmental Sciences* 99, pp. 311–323.
- Scheibel, H. and J. Porstendörfer (1983). "Generation of monodisperse Ag-and NaCl-aerosols with particle diameters between 2 and 300 nm". In: *Journal of Aerosol Science* 14.2, pp. 113–126.
- Schraufnagel, D. E. (2020). "The health effects of ultrafine particles". In: *Experimental & molecular medicine* 52.3, pp. 311–317.
- Schraufnagel, D. E., J. R. Balmes, C. T. Cowl, S. De Matteis, S.-H. Jung, K. Mortimer, R. Perez-Padilla, M. B. Rice, H. Riojas-Rodriguez, A. Sood, G. D. Thurston, T. To, A. Vanker, and D. J. Wuebbles (2019a). "Air Pollution and Noncommunicable Diseases: A Review by the Forum of International Respiratory Societies' Environmental Committee, Part 1: The Damaging Effects of Air Pollution". In: *Chest* 155.2, pp. 409–416.
- Schraufnagel, D. E., J. R. Balmes, C. T. Cowl, S. De Matteis, S.-H. Jung, K. Mortimer, R. Perez-Padilla, M. B. Rice, H. Riojas-Rodriguez, A. Sood, G. D. Thurston, T. To, A. Vanker, and D. J. Wuebbles (2019b). "Air Pollution and Noncommunicable Diseases: A Review by the Forum of International Respiratory Societies' Environmental Committee, Part 2: Air Pollution and Organ Systems". In: *Chest* 155.2, pp. 417–426.
- Schwarz, J. P., J. R. Spackman, R. S. Gao, A. E. Perring, E. Cross, T. B. Onasch, A. Ahern, W. Wrobel, P. Davidovits, and J. Olfert (2010). "The detection efficiency of the single particle soot photometer". In: *Aerosol science and technology* 44.8, pp. 612–628.
- Seinfeld, J. H. and S. N. Pandis (2016). *Atmospheric chemistry and physics : from air pollution to climate change*. Third edition. New York Academy of Sciences. Hoboken, New Jersey: John Wiley and Sons, Incorporated.
- Sparrow, E. M., J. P. Abraham, and W. J. Minkowycz (2009). "Flow separation in a diverging conical duct: Effect of Reynolds number and divergence angle". In: *International Journal of Heat and Mass Transfer* 52.13-14, pp. 3079–3083.
- Spurk, J. and N. Aksel (2008). *Fluid Mechanics*. 2nd ed. 2008. Springer Berlin Heidelberg.
- Stolzenburg, M. R. and P. H. McMurry (1991). "An ultrafine aerosol condensation nucleus counter". In: *Aerosol Science and Technology* 14.1, pp. 48–65.
- Sueper, D. (2024). *ToF-AMS Data Analysis Software Webpage*. Accessed: 3.7.2024. URL: http://cires1.colorado.edu/jimenez-group/wiki/index.php/ToF-AMS_Analysis_Software.
- Thermo Fisher Scientific Chemicals (2009). *Safety data sheet, Ag, 7440-22-4*. Revision 3.
- Thermo Fisher Scientific Chemicals (2012). *Safety data sheet, Zn, 7440-66-6*. Revision 3.
- Topas GmbH (2024). *ATM 220 Aerosol generator*. Accessed: 3.7.2024. URL: <https://www.topas-gmbh.de/en/products/generation/product/atm-220>.

- Topas GmbH (2025). *DDU 570/H Diffusion Dryer Unit*. Accessed: 10.1.2025. URL: <https://www.topas-gmbh.de/en/products/conditioning/product/ddu-570-h>.
- TSI Inc. (2024). *Aerosol Generator 3076*. Accessed: 3.7.2024. URL: <https://tsi.com/products/aerosol-generators-dispersers/polydisperse-generators/aerosol-generator-3076/>.
- Ulbrich, I. M., M. R. Canagaratna, Q. Zhang, D. R. Worsnop, and J. L. Jimenez (2009). "Interpretation of organic components from Positive Matrix Factorization of aerosol mass spectrometric data". In: *Atmospheric Chemistry and Physics* 9.9, pp. 2891–2918.
- Ulrich, G. D. (1971). "Theory of particle formation and growth in oxide synthesis flames". In: *Combustion Science and Technology* 4.1, pp. 47–57.
- Vu, T. V., J. M. Delgado-Saborit, and R. M. Harrison (2015). "Review: Particle number size distributions from seven major sources and implications for source apportionment studies". In: *Atmospheric Environment* 122, pp. 114–132.
- Wang, S., C. A. Zordan, and M. V. Johnston (2006). "Chemical characterization of individual, airborne sub-10-nm particles and molecules". In: *Analytical Chemistry* 78.6, pp. 1750–1754.
- Wang, S. C. and R. C. Flagan (1990). "Scanning electrical mobility spectrometer". In: *Aerosol Science and Technology* 13.2, pp. 230–240.
- Watson, J. G., J. C. Chow, and L.-W. A. Chen (2005). "Summary of organic and elemental carbon/black carbon analysis methods and intercomparisons". In: *Aerosol and Air Quality Research* 5.1, pp. 65–102.
- WHO (2021). *WHO global air quality guidelines: particulate matter (PM_{2.5} and PM₁₀), ozone, nitrogen dioxide, sulfur dioxide and carbon monoxide*. World Health Organization.
- Wiedensohler, A. (1988). "An approximation of the bipolar charge distribution for particles in the submicron size range". In: *Journal of aerosol science* 19.3, pp. 387–389.
- Williams, D. B. and C. B. Carter (2009). *Transmission Electron Microscopy: A Textbook for Materials Science*. 2nd ed. New York, NY: Springer Nature.
- Yanca, C. A., D. C. Barth, K. A. Petterson, M. P. Nakanishi, J. A. Cooper, B. E. Johnsen, R. H. Lambert, and D. G. Bivins (2006). "Validation of three new methods for determination of metal emissions using a modified Environmental Protection Agency Method 301". In: *Journal of the Air & Waste Management Association* 56.12, pp. 1733–1742.
- Zangmeister, C. D., C. D. Grimes, R. R. Dickerson, and J. G. Radney (2019). "Characterization and demonstration of a black carbon aerosol mimic for instrument evaluation". In: *Aerosol science and technology* 53.11, pp. 1322–1333.
- Zhang, X., K. A. Smith, D. R. Worsnop, J. L. Jimenez, J. T. Jayne, C. E. Kolb, J. Morris, and P. Davidovits (2004). "Numerical characterization of particle beam collimation: part II integrated aerodynamic-lens–nozzle system". In: *Aerosol Science and Technology* 38.6, pp. 619–638.